NASA/TM—2019-220046

New Test Rig to Measure Alternating Current Losses of Both Low and High Critical Temperature Superconductors

Jason Hartwig, Bryan Fraser, and Gerald Brown
Glenn Research Center, Cleveland, Ohio

Lee Kohlman
Langley Research Center, Hampton, Virginia

David Koci, Keith Hunker, and Cheryl Bowman
Glenn Research Center, Cleveland, Ohio

Phillip Schrum and David Matten
Forefront Engineering, East Pittsburgh, Pennsylvania

June 2019

NASA STI Program . . . in Profile

Since its founding, NASA has been dedicated to the advancement of aeronautics and space science. The NASA Scientific and Technical Information (STI) Program plays a key part in helping NASA maintain this important role.

The NASA STI Program operates under the auspices of the Agency Chief Information Officer. It collects, organizes, provides for archiving, and disseminates NASA's STI. The NASA STI Program provides access to the NASA Technical Report Server—Registered (NTRS Reg) and NASA Technical Report Server—Public (NTRS) thus providing one of the largest collections of aeronautical and space science STI in the world. Results are published in both non-NASA channels and by NASA in the NASA STI Report Series, which includes the following report types:

- TECHNICAL PUBLICATION. Reports of completed research or a major significant phase of research that present the results of NASA programs and include extensive data or theoretical analysis. Includes compilations of significant scientific and technical data and information deemed to be of continuing reference value. NASA counter-part of peer-reviewed formal professional papers, but has less stringent limitations on manuscript length and extent of graphic presentations.

- TECHNICAL MEMORANDUM. Scientific and technical findings that are preliminary or of specialized interest, e.g., "quick-release" reports, working papers, and bibliographies that contain minimal annotation. Does not contain extensive analysis.

- CONTRACTOR REPORT. Scientific and technical findings by NASA-sponsored contractors and grantees.

- CONFERENCE PUBLICATION. Collected papers from scientific and technical conferences, symposia, seminars, or other meetings sponsored or co-sponsored by NASA.

- SPECIAL PUBLICATION. Scientific, technical, or historical information from NASA programs, projects, and missions, often concerned with subjects having substantial public interest.

- TECHNICAL TRANSLATION. English-language translations of foreign scientific and technical material pertinent to NASA's mission.

For more information about the NASA STI program, see the following:

- Access the NASA STI program home page at http://www.sti.nasa.gov

- E-mail your question to help@sti.nasa.gov

- Fax your question to the NASA STI Information Desk at 757-864-6500

- Telephone the NASA STI Information Desk at 757-864-9658

- Write to:
  NASA STI Program
  Mail Stop 148
  NASA Langley Research Center
  Hampton, VA 23681-2199

NASA/TM—2019-220046

New Test Rig to Measure Alternating Current Losses of Both Low and High Critical Temperature Superconductors

Jason Hartwig, Bryan Fraser, and Gerald Brown
Glenn Research Center, Cleveland, Ohio

Lee Kohlman
Langley Research Center, Hampton, Virginia

David Koci, Keith Hunker, and Cheryl Bowman
Glenn Research Center, Cleveland, Ohio

Phillip Schrum and David Matten
Forefront Engineering, East Pittsburgh, Pennsylvania

National Aeronautics and
Space Administration

Glenn Research Center
Cleveland, Ohio 44135

June 2019

Acknowledgments

The authors wish to acknowledge our colleagues at the Wright Patterson Air Force Base, Larry Long and Dr. Rodger Dyson.

This report contains preliminary findings, subject to revision as analysis proceeds.

This work was sponsored by the Advanced Air Vehicle Program at the NASA Glenn Research Center

Level of Review: This material has been technically reviewed by technical management.

Available from

NASA STI Program
Mail Stop 148
NASA Langley Research Center
Hampton, VA 23681-2199

National Technical Information Service
5285 Port Royal Road
Springfield, VA 22161
703-605-6000

This report is available in electronic form at http://www.sti.nasa.gov/ and http://ntrs.nasa.gov/

New Test Rig to Measure Alternating Current Losses of Both Low and High Critical Temperature Superconductors

Jason Hartwig, Bryan Fraser, and Gerald Brown
National Aeronautics and Space Administration
Glenn Research Center
Cleveland, Ohio 44135

Lee Kohlman
National Aeronautics and Space Administration
Langley Research Center
Hampton, Virginia 23681-2199

David Koci, Keith Hunker, and Cheryl Bowman
National Aeronautics and Space Administration
Glenn Research Center
Cleveland, Ohio 44135

Phillip Schrum and David Matten
Forefront Engineering
East Pittsburgh, Pennsylvania 15112

Summary

This paper presents the design, development, operation, and test capabilities of a proposed superconducting coil testbed to measure alternating current (AC) losses at the NASA Glenn Research Center. Superconducting AC losses are important in the design of electric stators and rotors, power transmission lines, transformers, fault current limiters, magnets, and superconducting energy storage (not batteries). The new liquid-hydrogen-based rig will allow superconducting testing across a wide range of test parameters, including injected current up to 400 A, frequency (0 to 400 Hz), magnetic field (0 to 0.6 T), phase angle between induced voltage and injected current (–180° to 180°), coil coolant temperature (18 to 28 K), and AC power loss (5 to 30 W). While the target application of interest is 20 K superconducting MgB_2 (the only superconductor that can presently be made with low losses) stator coils for future electric machines, the rig can accommodate test articles (TAs) with straight wire, tape, cables, coils of any shape, any allowable combination of superconducting wire and fluid (e.g., yttrium barium copper oxide (YBCO) coils and liquid nitrogen), and AC or direct current (DC) testing. The new spin rig builds upon the existing Air Force spin rig through a more flexible mode of fluid control, a wider gap space (up to 10.2 cm) for TAs, and the ability to accommodate TAs over a wider range of operating temperatures (18 to 95 K) using liquid hydrogen, gaseous helium, or liquid nitrogen as the working fluid, thus supporting direct cooled machines below 77 K.

1.0 Introduction

This paper presents in detail the design, development, and operation of a new liquid-hydrogen- (LH_2-) based superconducting coil testbed to measure alternating current (AC) losses as a function of various operating parameters at the NASA Glenn Research Center. The new rig allows superconducting testing across a wide range of parameters, including injected current up to 400 A, frequency (0 to 400 Hz),

magnetic field strength (0 to 0.6 T), phase angle between induced voltage and injected current (–180° to 180°), coolant temperature (18 to 28 K), and AC power loss (5 to 30 W). While the target application of interest is magnesium diboride (MgB_2) stator coils for future electric machines, the rig can accommodate test articles (TAs) with straight wire, coils of any shape, and any allowable combination of superconducting wire and fluid from 18 to 95 K. For example, AC losses for yttrium barium copper oxide (YBCO) can be measured from 18 K up to the critical temperature or for MgB_2 from 18 to 28 K.

An outline of the paper is as follows: first, Section 2.0 (Background) provides motivation for constructing the new rig and presents test capabilities, including how the proposed LH_2 rig improves over an existing spin rig. The next section discusses possible superconducting coil TAs. The facility where testing occurs is also described. Then, each subsystem is systematically described, including the core test rig, power, fluids, instrumentation, data acquisition (DAQ), and controls subsystems. Appendix B, Appendix C, and Appendix D present the thermal, dynamic, and structural analysis, respectively. Appendix E outlines the seven different control system modes of operation. Finally, Appendix F presents hazards, interlocks, permissives, alarms, and shutdowns.

2.0 Background

2.1 Motivation

The primary application for the new superconducting coil rig is turboelectric aircraft propulsion systems, however, the rig can be used to test superconductors used in electric machine stators and rotors, transmission lines, transformers, fault current limiters, magnets, and superconducting energy storage. Recent studies (Refs. 1 and 2) have shown that introducing electrical components into aircraft propulsion systems may provide unmatched flexibility in coupling the power generation turbine to the fan propulsors, which may result in reduced noise, emissions, and fuel burn.

Figure 1 shows a concept-level diagram of the possible power distribution system that could be implemented into an aircraft. The dotted line distinguishes the electrical components from the existing components onboard the craft where the benefits of superconductivity may occur. Here, the fuel and air are mixed to combust inside a turbine engine, which is used to turn a mechanical shaft used to generate electricity. The electricity can then be distributed throughout the aircraft or used in the standard concentrated propulsion concept through the use of rectifiers, transmission lines, and inverters. Regardless of the configuration, the electricity is eventually used in a motor to turn a mechanical shaft connected to a fan to propel the aircraft.

Distributed propulsion concepts, such as the N3–X concept shown in Figure 2 or the D8 concept, have the potential to improve performance of the aircraft in three ways:

(1) Higher propulsion efficiency due to boundary layer ingestion (BLI). BLI allows ingestion of lower velocity flow near the airframe into the propulsors, reducing drag (Ref. 3). As shown in Figure 2, the propulsor is mounted so that slow flow is ingested, reenergized, and exhausted where the aircraft wake would traditionally be located.
(2) Higher propulsion efficiency due to increased bypass ratio. An electric driveline essentially decouples speed and inlet-to-outlet area ratios between the turbine and the fan, allowing for any number of fans to be driven by a single turbine. Furthermore, the fan pressure ratio and turbine-to-compressor speed ratios can be optimized independently.
(3) Lift-to-drag ratio improvements through wing flow circulation control, since propulsors can be mounted above, below, or embedded in the tube and wing aircraft configuration.

Jansen et al. (Ref. 2) quantified improved propulsion efficiency and also quantified the reduction in fuel consumption for all three of the previously mentioned ways.

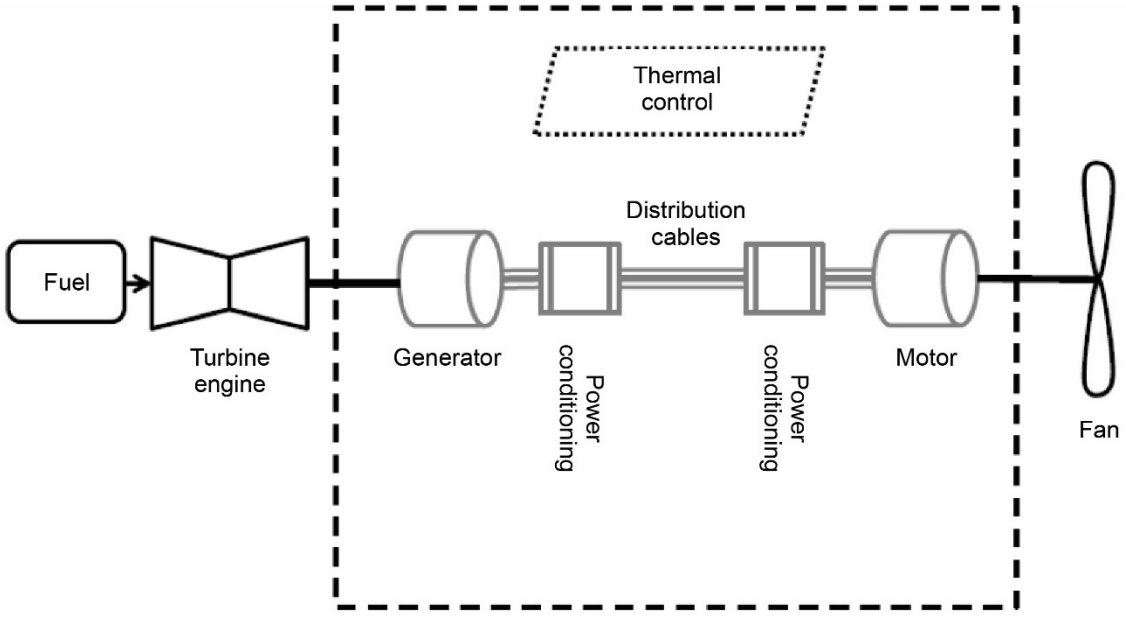

Figure 1.—Hybrid electric power distribution system, adopted from (Ref. 2).

Figure 2.—Distributed propulsion aircraft concept shown for illustrative purposes only.

Low AC loss superconducting coils having performance characteristics that are relevant to high power density, high-efficiency electric machines is a key technology development issue, but before fully superconducting electric drivelines are fully realizable, there are several key issues that need to be addressed. First, the addition of electrical components adds weight, complexity, and potential reliability issues to the system. Second, the increase in performance, higher power density, higher efficiency, and reduction in noise, emissions, and fuel burn is made possible through the use of superconducting electrical stators, rotors, and/or transmission lines; but this in turn requires that the electrical components operate at cryogenic temperatures due to the low critical temperatures (T_C) (highest temperature at which

a conductor exhibits superconducting behavior) of most superconductors. Therefore, the resultant addition of a cryogenic cooling system may also introduce added complexity and weight to the system due to the need for electrical cryocoolers and liquid- or gas-based cooling flow networks.

Third, there is currently only one superconductor that can deliver the high current density, compactness, and low losses that are necessary when exposed to the anticipated high AC current, magnetic fields, and frequencies. As a result, the superconducting machines of today typically have superconductors only in the rotor windings; the stators are wound with normal conductors such as copper, and operate at room temperature. One of the newer high-temperature superconductors for power applications is YBCO. Unfortunately, this superconductor has primarily been produced in the form of a thin, wide tape, which has prohibitively high AC losses. Another superconductor, bismuth strontium calcium copper oxide (BSCCO), has been produced in multifilamentary form, but without the fineness of filaments and high resistivity needed to yield low AC losses. Both YBCO and BSCCO possess useful current-carrying capacity at temperatures between 20 and ~60 K (even though the T_C of each superconductor is higher). Based on preliminary analysis, a third superconductor, MgB_2, is the closest superconductor that appears amenable to delivering the high current density, compactness, and low AC losses needed. However, the T_C is only 39 K, and large quantities of low AC loss MgB_2 superconducting wire have never been produced in a sufficient quantity to perform statistically significant testing to date. Therefore, a fourth issue is the lack of knowledge and experience in fabricating and testing large quantities of low AC loss MgB_2 superconducting wire.

The fifth and final issue, and obviously the largest hindrance, is that no test rig currently exists with which to evaluate low AC loss superconducting coil performance in the presence of AC varying currents, fields, and frequencies. No rig exists to provide experimental data to validate AC loss predictive models. Various rigs do exist in the world to test direct current (DC) superconducting coil performance such as in Reference 4, but this is a liquid-nitrogen- (LN_2-) based system, and it cannot produce temperatures needed for MgB_2 testing. Another rig concurrently being developed is the Integrated Cryogenically Cooled Experiment (ICE) Box. This rig uses cryocoolers to maintain temperatures as low as 9 K on a flat copper mounting surface. However, this rig cannot currently produce AC varying frequencies from a spinning rotor. There is one test rig that can simulate required AC fields and frequencies called the spin-around-magnet (SAM) rig (Ref. 5), but it too is an LN_2-based system, and therefore limited to testing at 78 K or warmer (although the system could possibly be configured for liquid helium (LHe) service to achieve MgB_2 temperatures, LHe is quite expensive). Furthermore, it is limited in the input current (<38 A), and it relies on boiloff calorimetry, which can incur significant error if successive, overlapping flowmeters are not used to measure boiloff.

2.2 Alternating Current (AC) Losses

The focus of the new experimental rig is on obtaining AC loss data in conditions relevant to the superconducting community. Experimental AC loss data is needed not only for the design of superconducting electric motors and generators, but also for power transmission lines, transformers, fault current limiters, magnets, and superconducting energy storage systems.

AC loss is defined as the energy dissipation in superconductors due to AC currents and externally applied magnetic fields. There are several different contributing processes:

$$W_{\text{total}} = W_{\text{hysteresis}} + W_{\text{eddy current}} + W_{\text{coupling}} + W_{\text{transport}} + W_{\text{other}} \quad (1)$$

where

$$W_{\text{hysteresis}} = \left(\frac{8}{3\pi}\right)\left[J_C\left(B,T\right)Bf\right]d_f l V_w \tag{2}$$

$$W_{\text{eddy current}} = \left(\frac{\pi^2}{2\rho_n}\right)\left(d_w Bf\right)^2\left(1-l\right)V_w \tag{3}$$

$$W_{\text{coupling}} = \left(\frac{1}{2\rho_n}\right)\left(t_p Bf\right)^2\left(1-l\right)V_w \tag{4}$$

$$W_{\text{transport}} = \left(\frac{\mu_0}{4}\right)f_e d_f^2 J_C^2\left[\left(1-\frac{I_T}{I_C}\right)\ln\left(1-\frac{I_T}{I_C}\right)+\frac{I_T}{I_C}-\frac{1}{2}\left(\frac{I_T}{I_C}\right)^2\right]lV_w \tag{5}$$

where

d_f is superconducting filament through wire diameter
d_w is wire diameter
f_e is injected current frequency
I_C is critical current
I_T is injected transport current
J_C is critical current density
l is fraction of wire cross section made of superconducting filament
t_p is twist pitch of superconducting filament
V_w is wire volume
W_{other} includes twist-pitch losses, resistive losses, dynamic losses, and self-field losses
ρ_n is transverse matrix resistivity
μ_0 is permeability of free space

Note that V_w is the volume of the entire wire for the whole motor or generator. Also, note that a time-varying field alone will yield lower losses in the superconductor than a time-varying field of the same magnitude that is also rotating. Furthermore, the phase angle of the transport current also affects the losses.

Of the terms in Equation (1), coupling will likely dominate. Hysteresis can be comparable if the superconducting filaments are not small enough. While also proportional to the magnetic field squared, eddy current losses are generally small. Transport losses are small if the wire has no magnetic components, which is the goal of recent superconducting wire manufacturers. The self-field losses are small if the self-field is small relative to the external field; this term usually only matters in very short samples.

2.3 Test Capabilities

Examination of Equations (1) to (5) indicates that for a fixed superconductor, the primary AC loss terms are a function of frequency, f, peak magnetic field, B, and injected transport current, I_T. The first and third of these experimental parameters can be adjusted in the new rig. The peak field, B, can be varied slightly by test sample position in the available annular space. Thus, the new rig will provide a means of repeatedly subjecting coil packs to representative electrical (current and voltage), thermal (cooling and

environmental), electromagnetic (field and frequency), and mechanical (AC-induced cyclic loading) conditions representative during aircraft turboelectric propulsion system operation. Specifically, the superconductors can be exposed to a time-varying and geometrically varying magnetic field while being actively cooled to retain superconducting properties. Furthermore, superconducting coils can be injected with a representative AC operating current of any desired waveform, which will impart a realistic, cyclic mechanical loading on the superconductors. Such a testbed allows electromagnetic, electrical, thermal, and mechanical performance aspects of superconductors to be evaluated under relevant conditions so that suitably performing, robust superconductors may be reliably produced and the performance predicted.

Consequently, the testbed provides the capability to simultaneously control the time-varying and geometrically varying magnetic field, injected current, and the flow conditions of the superconductor coolant for any TA. This permits superconductor losses to be measured under realistic operating conditions. It also yields a more comprehensive understanding regarding the design, fabrication, and operation of superconductors.

The new LH_2-based rig allows testing across a wide range of parameters, including current amplitude (0 to 400 A), frequency (0 to 400 Hz), phase angle between induced voltage and injected current (–180° to 180°), magnetic field (0 to 0.6 T), superconductor coolant temperature (18 to 95 K), and AC power loss (5 to 30 W). The rig can conduct AC or DC testing. While the target application of interest is 20 K superconducting MgB_2 stator coils for future electric machines, the rig can accommodate TAs with straight wire, coils of any shape, and any allowable combination of superconducting wire and fluid (e.g., YBCO coils and LN_2) according to size limitations laid out in Section 3.0. While the $B_{max}*f$ range is approximately the same, the new rig expands upon the existing Air Force spin rig in the following ways:

(1) The new rig has a larger gap space, 5.08 cm (2 in.) with provision to go to 10.16 cm (4 in.), which provides more room to test larger samples, and a wider range of samples (coils, straight wire, cables, and tapes).
(2) The new rig has a wider temperature range over which to test samples. The new rig is not locked into a low range of fluid saturation temperatures by low design pressures. The new rig uses a subcooling system and a higher rated flow system and storage vessel, which allows independent control of fluid temperature and pressure.
(3) The new rig can accommodate the 20 to 30 K range needed to study MgB_2, the only superconductor, which can presently be made with low AC losses.
(4) The extra gap space permits adaptation of the rig to use pressurized GHe as a coolant, which expands the capability to run tests in the 40 to 70 K range.
(5) The LH_2 rig can easily be converted to an LN_2 rig to permit testing in the 68 to 95 K range.

What follows is a description of the type of TAs that the new LH_2-based AC loss rig can accommodate.

3.0 Test Articles (TAs)

As mentioned previously, the new test rig can accommodate superconducting wires, cables, tapes, and coils that fit within the allowable size limits outlined in Section 5.0, Core Rig. In accordance with the size envelope of the core test rig, the following is a list of specifications for any TA:

- Must fit in an arc-shaped volume roughly 55.3 cm (21.775 in.) long, with an inner diameter (I.D.) of 31.12 cm (12.25 in.), outer diameter (O.D.) of 37.47 (14.75 in.), and included angle of 60°
- Must include connections for fluid inlet and outlet

- Must accommodate mechanical connections at each end
- Must fit through top mounting plate
- Fluid flow must be single phase throughout to ensure low-pressure drop
- Must be a nonmagnetic and nonelectrically conductive housing

The following is an example of types of superconductors that can be tested using the new rig. Emphasis in the near-term testing is on TAs that are in some way representative of superconducting stator coils that might be used in a turboelectric propulsion system. Here, testing is performed on two primary TA configurations: type A, having just straight lengths of superconductor, and type B, having multiple turns of superconductor (i.e., coils). The main difference between types A and B is only geometrical considerations.

Two different type B coil geometries can be explored: flat (F) coil and saddle (S) coils having curvature. Types A and B TAs can be further broken into two subcategories: (i) those where coolant is in direct contact with the superconductor and (ii) those where the coolant is not in direct contact with the superconductor. Furthermore, two subcategories of type i TAs exist: (a) those with coolant flow parallel to the axis of the wire and (b) those with coolant flow normal to the axis of the wire. In the near term, only types 1.A.i.a., 1.B.F.i.a., and 1.B.S.i.a. TAs will be considered. These TA options are illustrated in Figure 3.

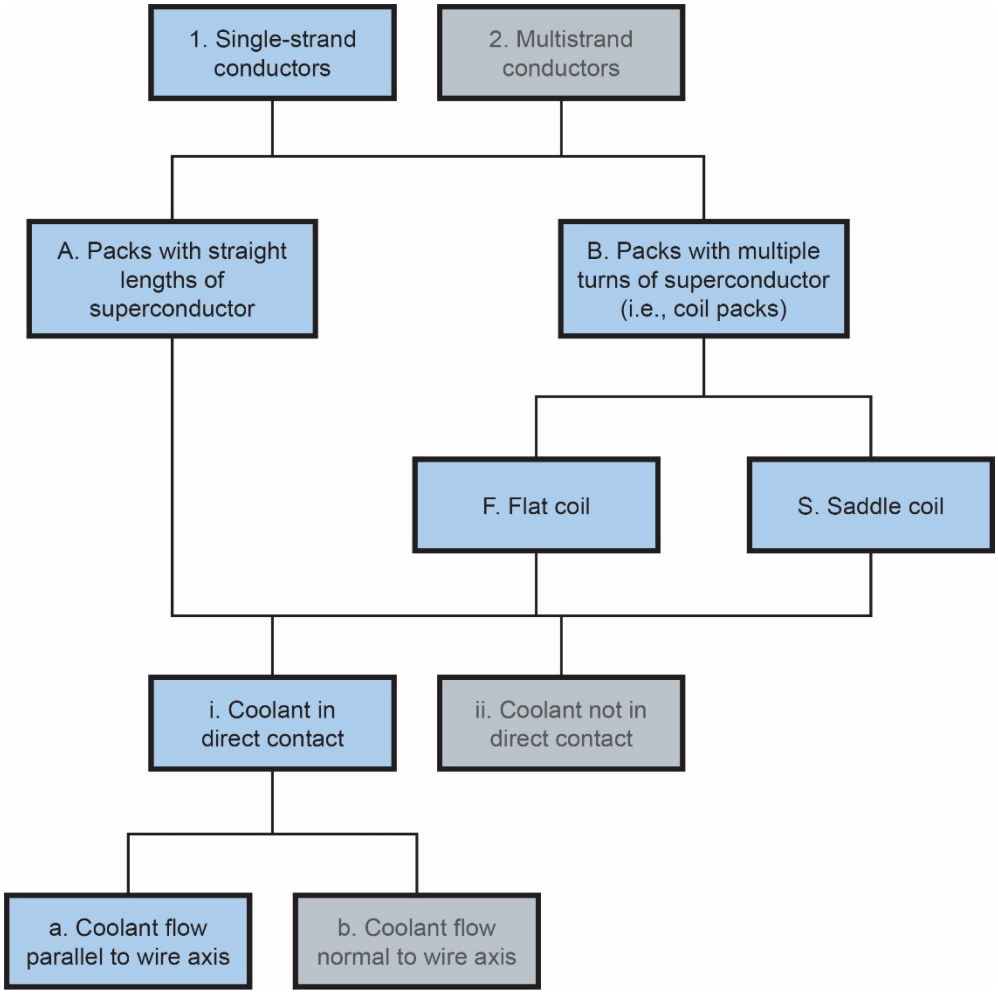

Figure 3.—Types of superconducting coil packs supported by new test rig.

For each of the TA types, a variety of different packs can be tested (i.e., combinations of different wire diameters, center-to-center spacing, housing materials, methods of supporting and/or fixing the superconductor, and number of layers of superconductor). Type A packs offer a simplified construction and a simple means of assessing wire cooling effectiveness, while still being able to measure AC losses at zero transport current, which allows zeroing in on the hysteresis, eddy current, and coupling loss terms in Equation (1). Straight lengths of conductor are cleaner from an analysis perspective because of the removal of the spatial location and orientation dependence of heating in end turns. Additionally, type A packs avoid the issue of strain tolerance in bent wires. The packs are simpler to produce, including related handling considerations. Multiple straight lengths of conductor can be incorporated into a single TA, perhaps up to 100.

Type B coil packs can be used to assess wire cooling effectiveness, AC losses with transport current, and the coil pack mechanical durability. These coil packs could start out simple while maintaining some degree of relevance to the future application (e.g., flat, racetrack-type winding configuration), and evolve to being more complex with a much larger degree of relevance to the future application as fabrication and testing experiences grow (e.g., saddle coils). The winding configuration can be such that it cancels most of the voltage generated by the changing magnetic field. Type B coil pack testing can be used to investigate heating of the wire caused by alternating magnetic fields with and without transport current in the wires and self-generated fields. AC losses are estimated to be in the 1- to 30-W range. Approximately 90 percent of these losses are expected to be the result of exposure to a time-varying magnetic field and 10 percent the result of the injected current.

Figure 4 shows the buildup of an MgB_2 dual coil pack. Table 1 outlines design features of the first few MgB_2 samples to be tested. A single layer of wire with multiple turns is heat treated, and then the windings are transferred to a G10 former. The grooved G10 former is used to house the coils. In this configuration, it is possible to test two coils within a single TA; the two coils can be inserted and then sealed with adhesive and the G10 plates. The two superconducting coils are joined by a nonsuperconducting piece of copper, which is not anticipated to affect AC loss measurements because it is located in an area where the field is quite low.

Figure 5 shows the assembled type A straight wire sample. Samples are constructed from layers of G10 with a cryogenic rated structural adhesive film used to bond the layers together. Where possible, the bond and sealing surfaces are kept flat to minimize distortion to the bond layer. The wire is sealed in shallow grooves in the G10 and tacked using superglue to hold the wire in place during fabrication. Film adhesive is used on the side opposite the wire grooves to bond the wire in place. Coolant fluid flow channels are formed by spaces between the wires and also cut into the groove side of the G10 structure. Fluid is routed along the channel formed between the top and middle G10 layers, past the wire, and back through a channel formed between the middle and bottom G10 layers. Fluid fittings are captured between the top and middle layers and bonded in place with film adhesive on both sides of the captured flange. The microchannel formed allows coolant to flow across the wires, but at a reasonable single-phase pressure drop.

Figure 6 shows the assembled type B coil pack. Here, the packs are double-sided and fluid flows in one end, through the coils on each side, and out the other end. Electrical connections and fluid ports will be on the same end.

Figure 7 shows a third type of coil pack that can be used for calorimetry calibration before AC loss measurements are taken. This coil pack is used to ensure that the power input into the fluid from a heater is proportional to the enthalpy change of the fluid so that confidence is improved when testing AC loss heat input into the fluid. All wires are omitted from the active area. A small amount of additional material

is removed from the upper end of the flow path. One or two small resistive heaters are placed in the upper flow path and a crossover jumper is used.

Note that even the type B coil packs are planar, flat, racetrack type coils; they are not three-dimensional (3D) saddle coils expected in a final electric machine. Furthermore, single-phase testing will not account for the overlapping stator coils in real machines; in a machine, overlapping coils will experience the rotor field and fields from coils in the other phases. The rig is not being designed with any particular machine in mind, but rather as a multipurpose testbed for superconducting components.

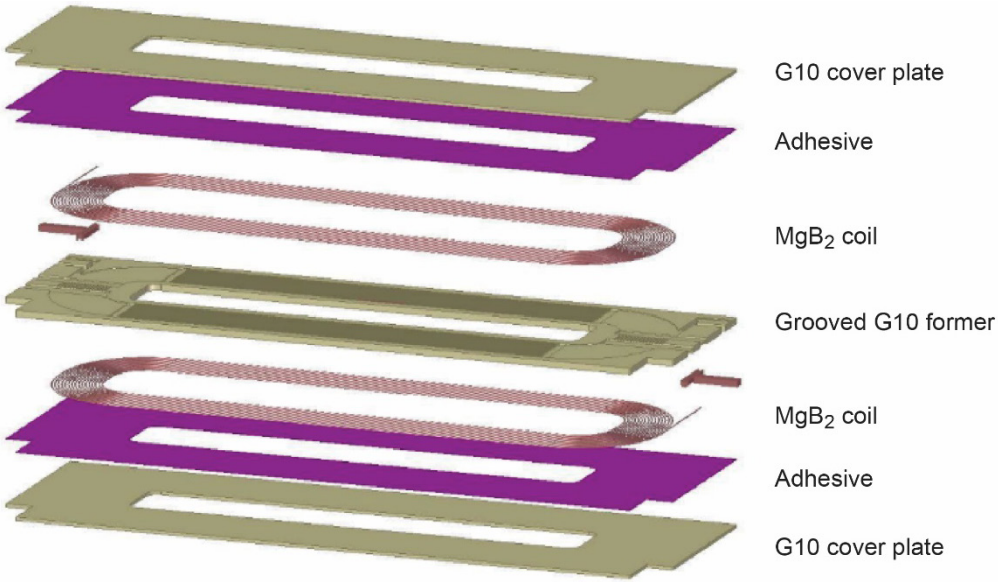

Figure 4.—MgB2 coil sample.

TABLE 1.—DESIGN FEATURES OF FIRST MgB_2 COIL SAMPLES

Coil no.	No. of filaments	Barrier	Mono sheath (matrix)	Outer multisheath	Center filaments	Twist pitch, mm	Diameter, mm	d_{eff}[a], μm
1	54	Nb	Cu10Ni	Cu30Zn	Cu10Ni	10	0.85	45
2	54	Nb	Cu10Ni	Cu30Zn	Cu10Ni	5	0.85	45
3	78	Nb	Cu10Ni	Cu30Ni	Cu10Ni	5	0.85	35
4	78	Nb	Cu10Ni	Cu30Ni	Cu10Ni	10	0.85	35

[a]Effective diameter.

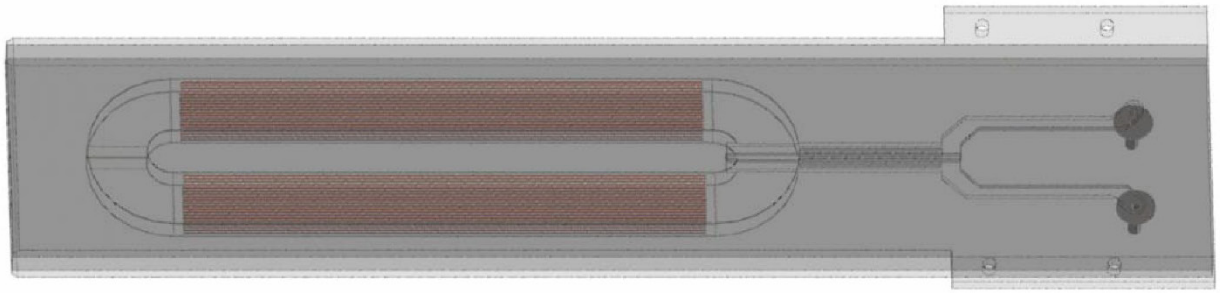

Figure 5.—Type A sample.

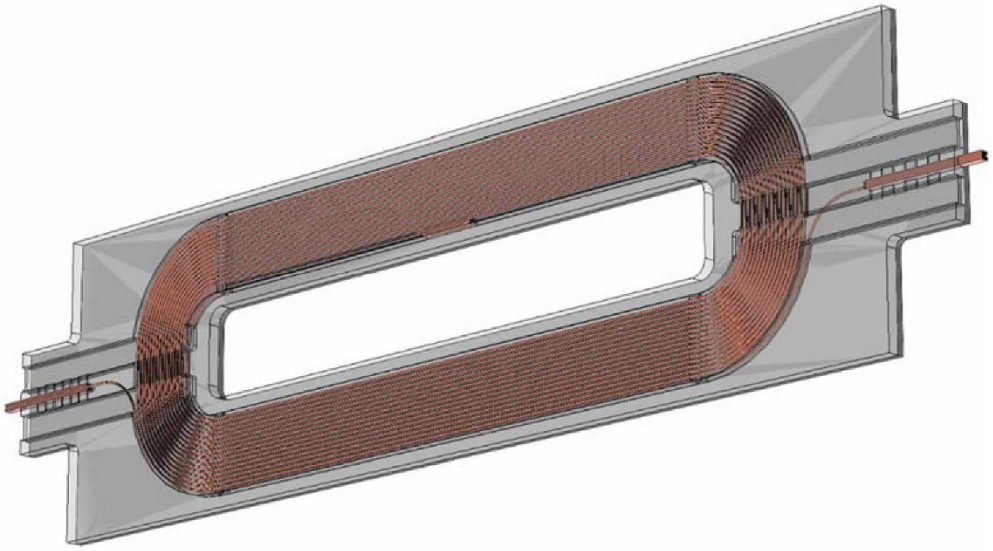

Figure 6.—Type B coil pack.

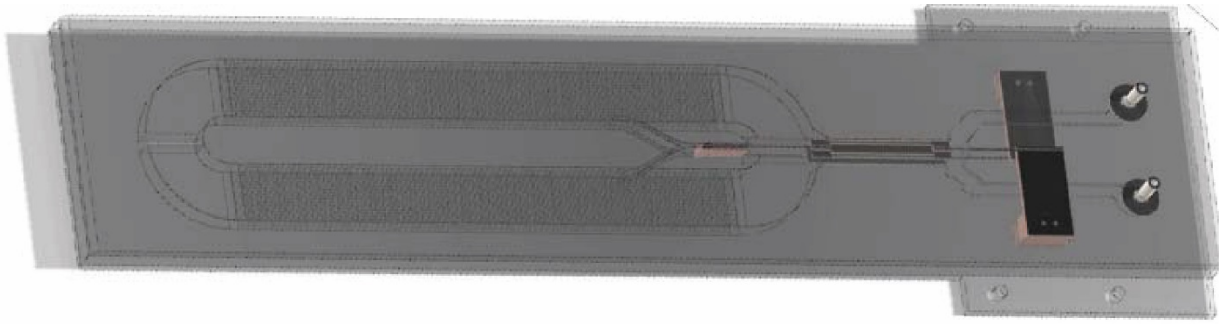

Figure 7.—Calorimetry calibration coil pack.

4.0 Facility

Testing will take place at the Small Multipurpose Research Facility (SMiRF) at Glenn in Cleveland, Ohio, as shown in Figure 8. Figure 9 outlines the high-level system diagram. The SMiRF is located within a National Fire Protection Agency (NFPA) 70 Class 1, Division 2, Group B boundary. The new LH_2-based AC loss test rig will use many existing interfaces, including electrical power, DAQ, and a fluids system, including LH_2, LN_2, GHe, and GN_2 fluids system control. The core test rig is anchored into place by threaded inserts embedded into the first floor concrete. The core test rig, fluids system, and fluids system control are located inside the main SMiRF facility, while the control system, driver motor, driver motor braking system, DAQ, and power supply subsystems are located in the shop area adjacent to the main SMiRF facility. LH_2 is supplied by a large roadable dewar, H91, parked outside the facility. Meanwhile, the core test rig and fluids system will occupy the open floor space shown in Figure 8.

Figure 8.—The Small Multipurpose Research Facility. Core test rig, fluids system, and fluid temperature control systems will be located on floor in front.

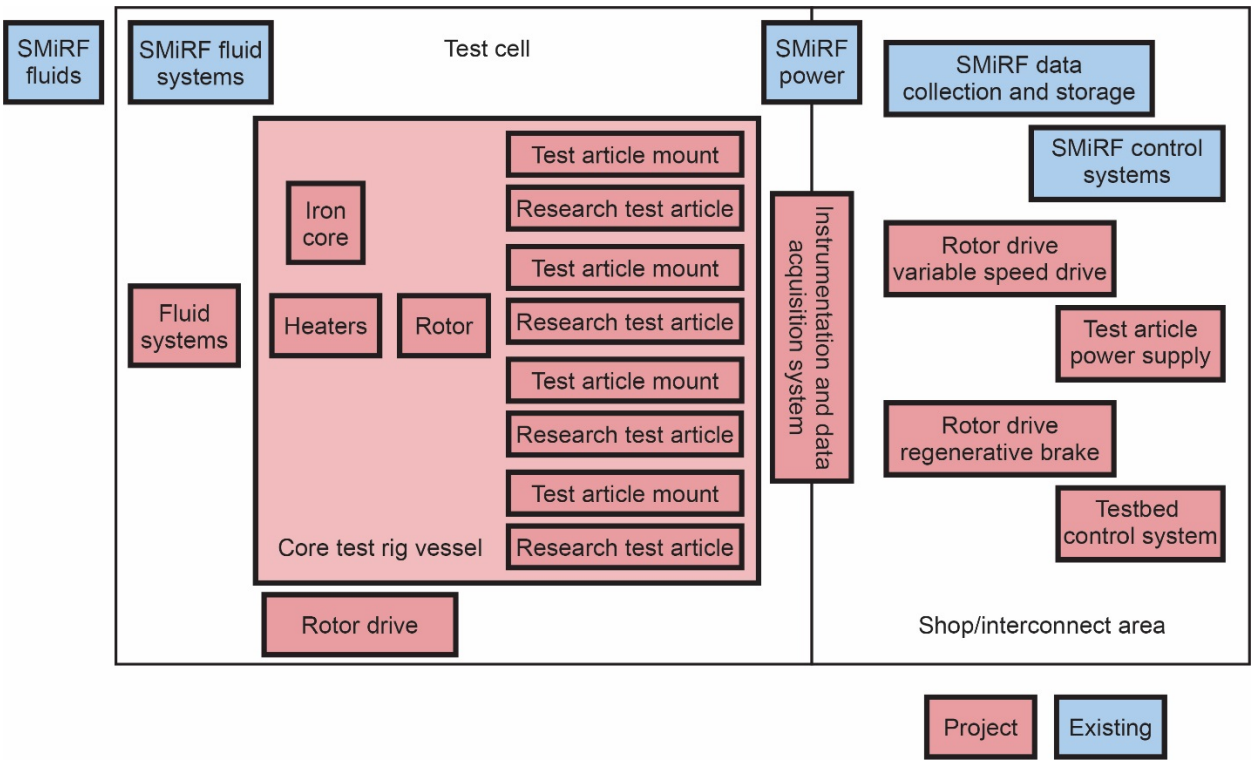

Figure 9.—High-level system diagram, where SMiRF is Small Multipurpose Research Facility.

5.0 Core Rig

The core rig is the main part of the new AC loss test rig and comprises the vessel, rotor, rotor drive, back iron, TA mount, heaters, and radiation shields. The core rig can accommodate TAs spanning up to one-half pole pitch (the center-to-center distance between neighboring poles of opposite polarity.) The core rig can accommodate TAs as specified in Section 3.0. The following is a detailed description of each subsystem of the core rig.

5.1 Vessel

The cryogenic rated vessel used to house the TAs is shown in Figure 10 to Figure 12. The exterior of the completed vessel is shown in Figure 13. The vessel supports the TAs, rotor, back iron, and components for testing. The maximum allowable working pressure of the vessel is 194 kPa (28.1 psia). It is evacuated to below 10^{-5} torr to minimize gas conduction heat transfer to the TAs. The vessel can accommodate up to four TAs at one time. All metallic components are bolted to the vessel, and the vessel is fully grounded.

Figure 10 illustrates a cutaway of the core test rig and the mechanical layout near the rotor and vessel interface. Figure 11 shows the mechanical layout for the core test rig, and Figure 12 shows the mechanical layout at the vessel lid. The rotor drive motor attaches to a mount outside the rig and interfaces with the vessel bottom plate through a Ferrofluidic® (Ferrotec Corporation) seal. A shaft connects to the spinning rotor inside the vessel where bearing housings and angular contact bearings hold the shaft in place. The motor is mounted to the bottom plate and then the skirt is mounted to the bottom plate. The rotor is attached to lubricated bearings on the top and bottom using a light press fit and then constrained in place using lock washers and lock nuts. The bearing housing is then attached to the bottom plate. An LN_2-cooled cylindrical back iron is used to terminate the magnetic field and is also mounted to the bottom plate using invar and steel rings and clamps. The back iron is cooled to reduce radiation heat leak into the TAs. It is not shown, but variable compression ratio (VCR) fittings are fastened to the back iron to supply LN_2. A middle plate is then assembled to the bottom cylinder that is used to shield the TAs from fluid and power feedthroughs from above. LH_2 is used to cool the power leads and reduce parasitics into the vacuum space below. TAs are installed in the vacuum space. Power leads connect to the TAs to provide injected current and voltage taps are provided to measure voltage. Fluid fittings connect to the TAs to provide coolant for the superconductors. The pressure and temperature at both inlet and exit of the TAs is measured using vacuum-rated pressure transducers and Cernox® (Lakeshore Cryotronics, Inc.) temperature sensors.

Next, the top plate and cylinder are mounted to the rig. Feedthroughs include bayonets used to supply cryogen, vent, burst disk, vacuum pump, vacuum sensors, instrumentation, voltage, and current. The pink shaded region between the outer vessel wall and the outer thin shell is filled with air to complete the rig as shown in Figure 14. For fabrication and construction, the American Society of Mechanical Engineers Boiler and Pressure Vessel (ASME B&PV) Code is employed.

5.2 Rotor

The rotor is a 30.5-cm- (12-in.-) O.D., 22.9-cm- (9-in.-) tall permanent magnet assembly configured as an eight-pole Halbach array driven by a motor and a controller. Figure 14 shows a cutaway diagram of the rotor. The rotor is warm but has a mirror finish to minimize radiation. The test rig rotor is rotationally positioned and lockable using a high-resolution encoder on the motor; braking is used to lock the rotor. SKF 6210 deep groove ball bearings are used at the upper rotor surface as shown in Figure 15. The bearings use grease designed for vacuum applications. The bearings are assembled with a very light slip fit, allowing them to move vertically. Smalley wave springs preload the bearings to prevent bearing slippage. Meanwhile, at the bottom rotor surface, SKF 7210 BEGBP angular contact bearings are assembled with a light press fit and preloaded against each other in a back-to-back arrangement.

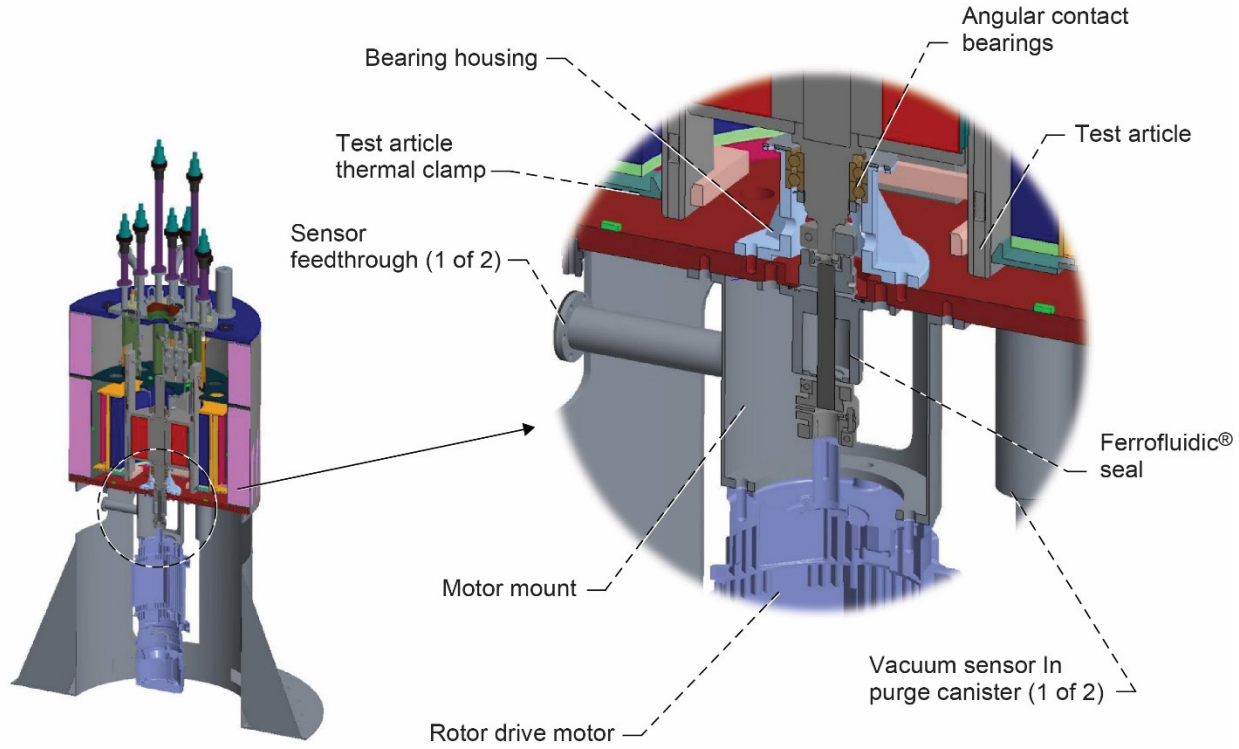

Figure 10.—Core test rig near rotor and vessel interface mechanical layout, where TA is test article.

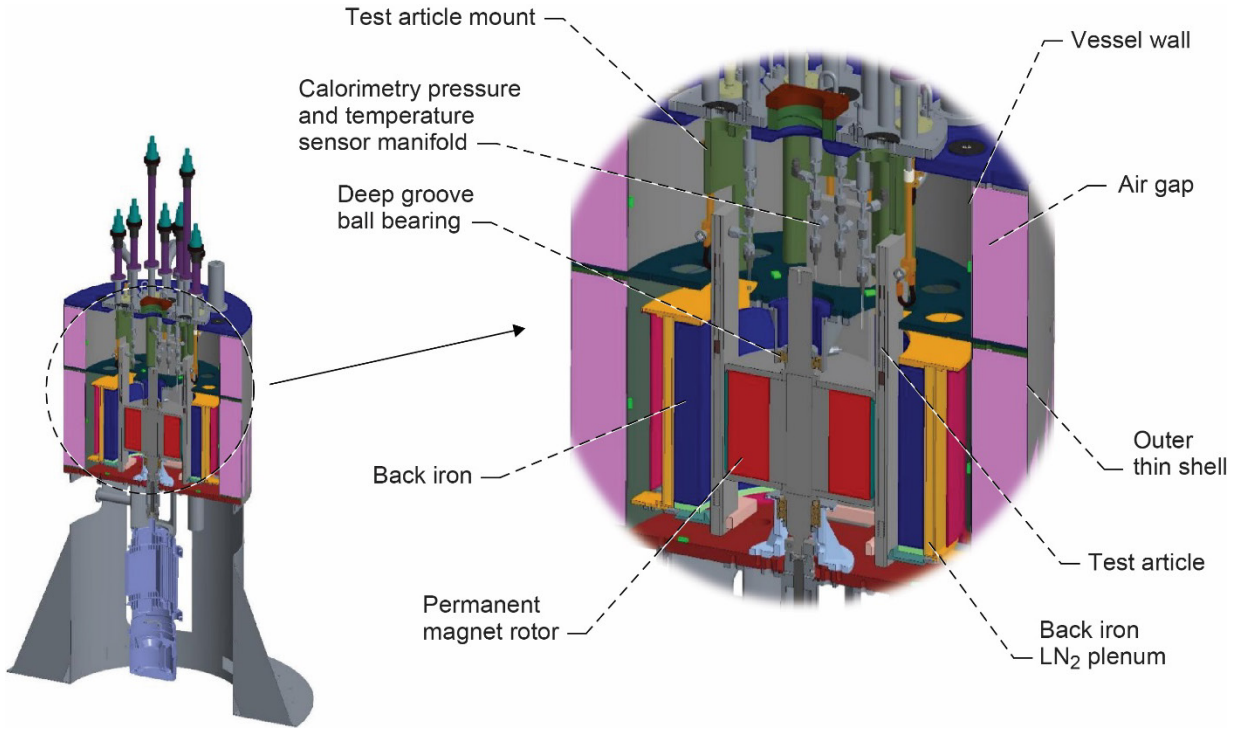

Figure 11.—Core test rig and inner vessel mechanical layout.

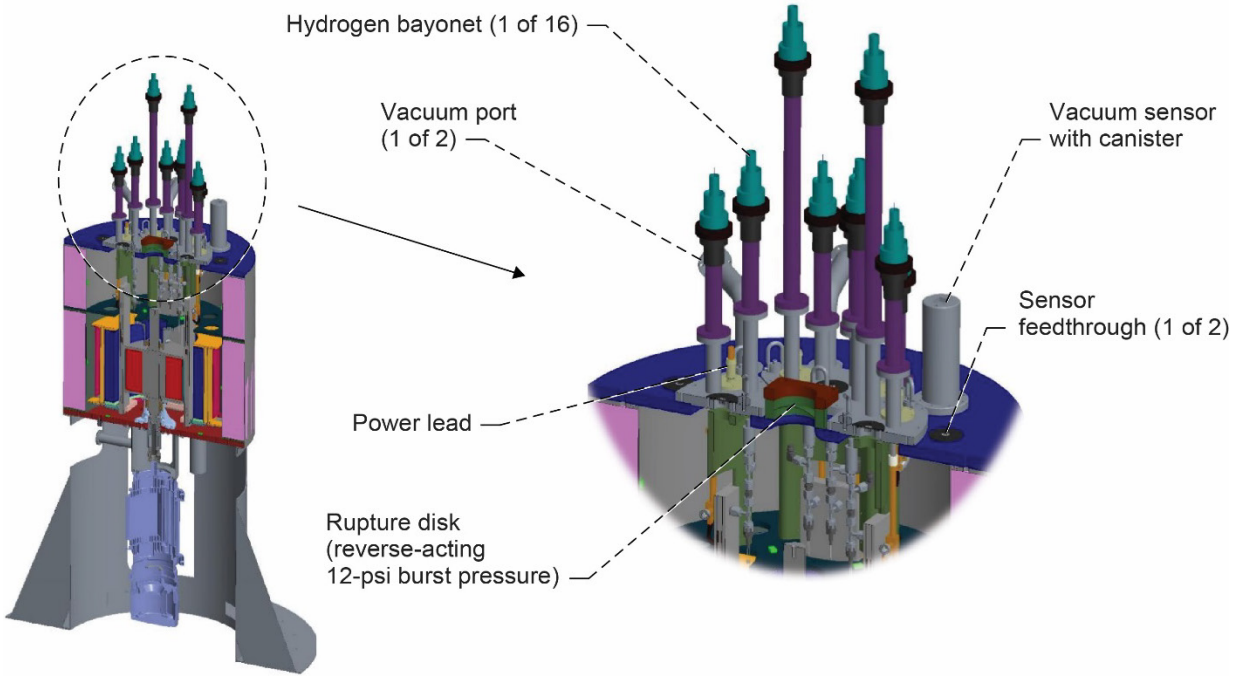

Figure 12.—Core test rig at vessel lid mechanical layout.

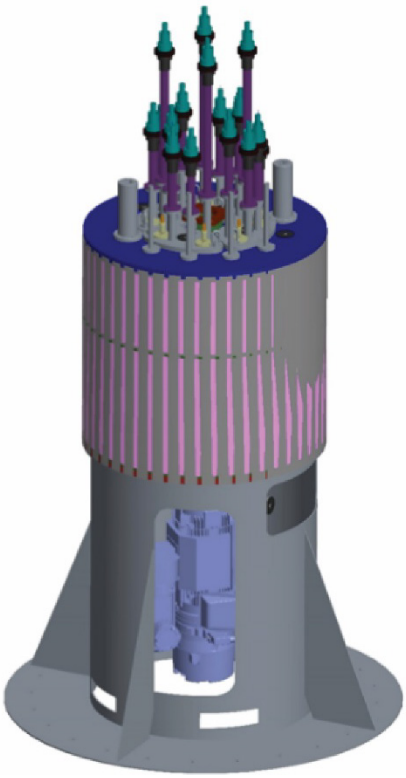

Figure 13.—Completed core rig with outer cryogenic vessel.

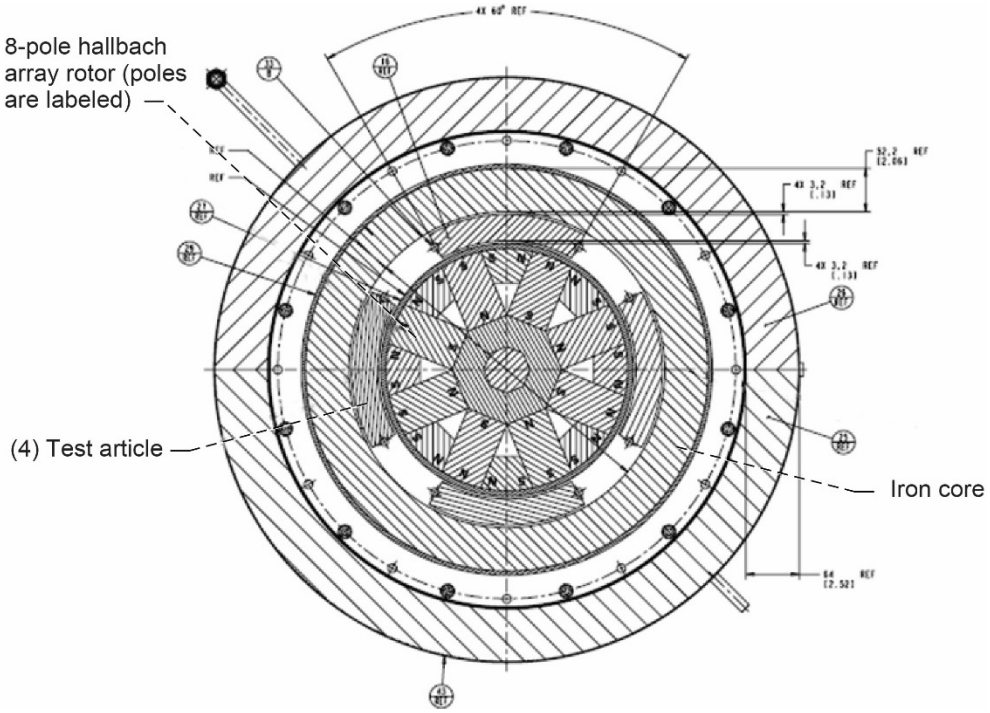

Figure 14.—Rotor cutaway diagram.

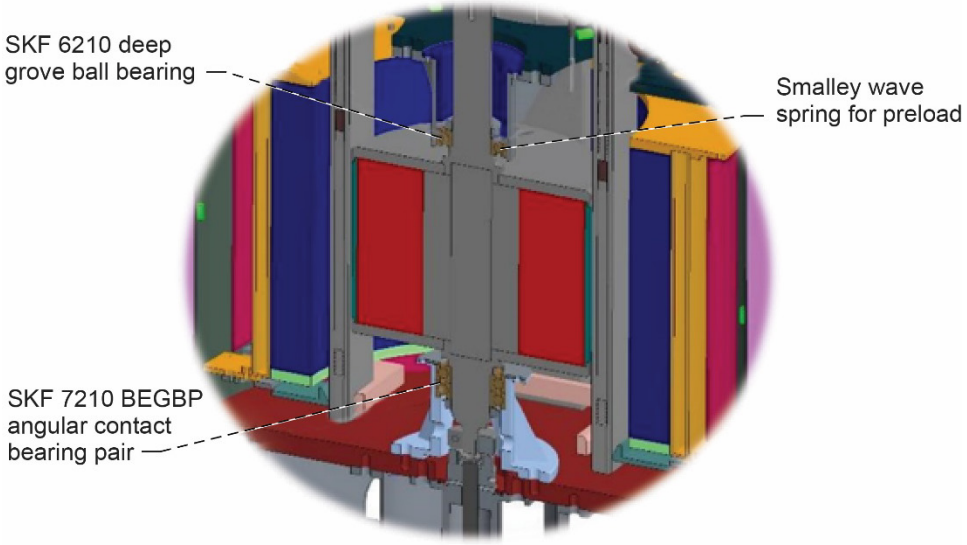

Figure 15.—Rotor bearings.

5.3 Rotor Drive

The rotor drive system consists of an electric motor, a variable frequency drive (VFD), and protection components. As shown in Figure 13, the entire rotor drive system is external to the vessel and sized to bring the rotor to maximum speed in just a few minutes. The motor is certified as Canadian Standards Association (CSA) Class 1, Division 2, Group A, B, C, D, T3 (473 K). It is capable of continuous operation at rotor speeds from 100 to 6,000 rpm. A means of braking the rotor from 6,000 to 0 rpm in less than 2 min is incorporated using a regenerative braking system. Furthermore, the rotor drive system

incorporates a means of rotationally positioning the rotor and holding that position to support 0-rpm tests. Note that the shaft speed of a large ducted fan speed is typically 2,000 to 3,000 rpm and the shaft speed of a high-speed generator may be as much as 8,000 rpm. The rig is designed for a 6,000-rpm maximum, so it is between the two ranges.

The bearing lubricant can last for ~2,800 h of run time at 6,000 rpm without needing relubrication. Operation at lower revolutions per minute increases duration between lubrication intervals; 5,000 rpm corresponds to 4,200 h of continuous run. Meanwhile, the drive system is suitable for at least 2,600 starts.

5.4 Back Iron

The back iron shown in Figure 16 is a 40.6 cm (16 in.) I.D., 35.6 cm (14 in.) tall, 205 kg magnetic shield of 1,500 stacked 0.178-mm (0.007-in.) electric steel laminations with an epoxy binder/insulation. It is located outside (behind) the TAs in Figure 14. The back iron gap provides a 5.08-cm (2-in.) gap for mounting TAs, and there is provision for substituting a back iron stack that provides up to a 10.2-cm (4-in.) gap to allow for considerably larger TAs as well as to permit testing in different strength magnetic fields. An LN_2 bath is located outside (behind) the back iron to maintain the temperature of the back iron to 80 K and reduce the parasitic heat leak into the TAs. The temperature is maintained in a boiling state by controlling the pressure. A capacitance probe is used to ensure the liquid level is maintained and to determine if refill is needed. Heaters are attached to the back iron to reduce warmup times between tests.

5.5 Test Article (TA) Mounts

The TA mounts are standardized means of mechanically securing any TA. The vessel has four openings, which fit and seal the standardized test mounts. As shown in Figure 17, the mounts have connections and tubing to supply LH_2 coolant to the TAs. As shown in Figure 18, the mounts also provide power leads to supply injected current to the TA up to 400 A. TA mounts also provide the TA instrumentation and feedthroughs and interface with the middle plate above. Mounts are configured in such a way that the instrumentation wires are sufficiently isolated from any source of electromagnetic noise; the tubing and power leads are outside the magnetic field.

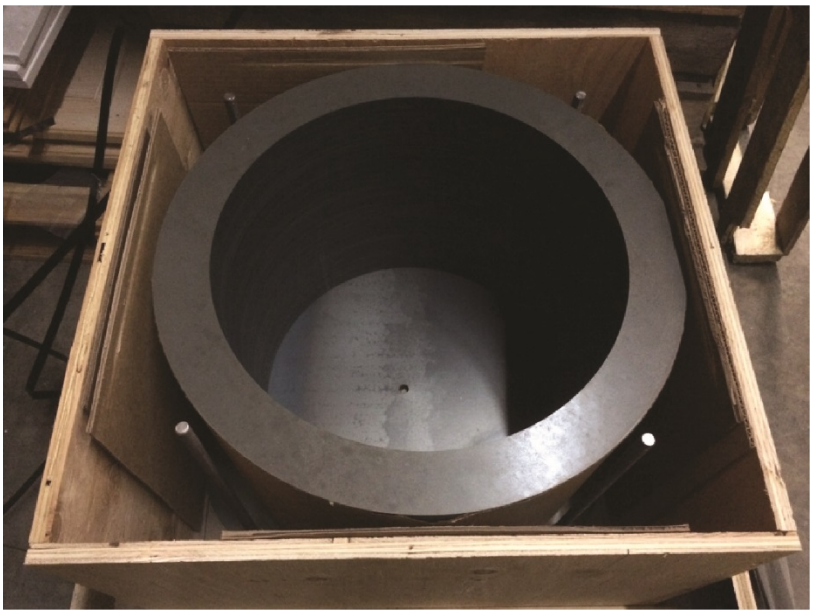

Figure 16.—Back iron.

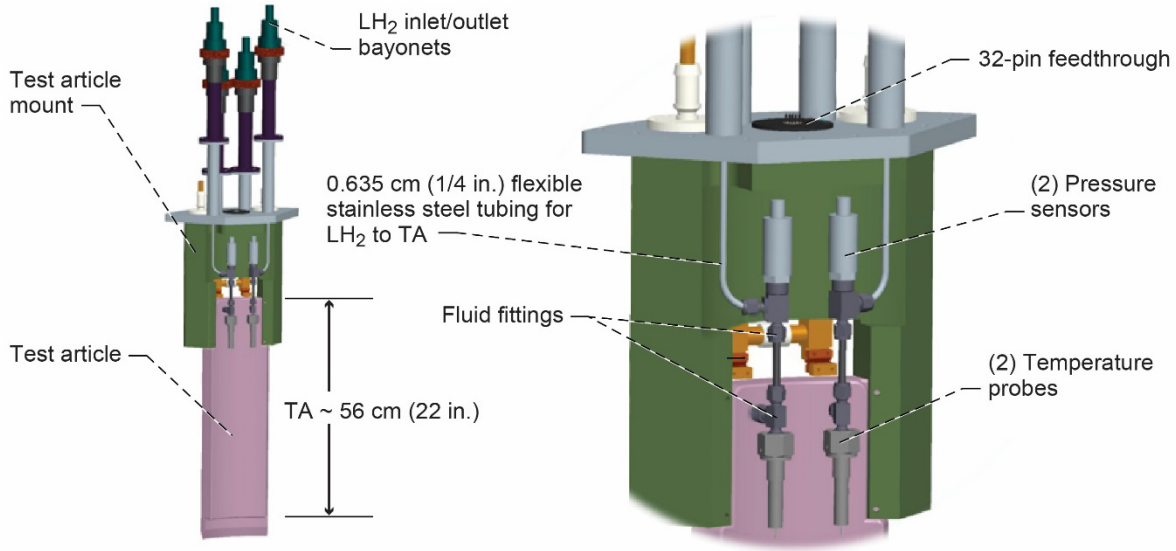

Figure 17.—Test article mounts and fluid connections.

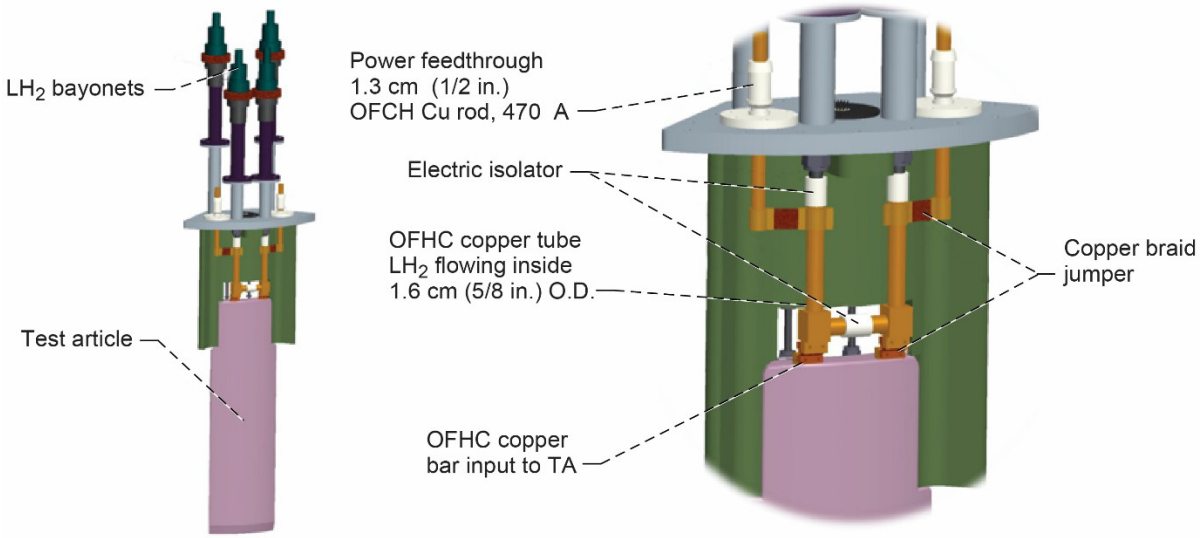

Figure 18.—Test article mounts and power connections. Power feedthroughs use oxygen-free high thermal conductivity copper (OFHC).

5.6 Thermal Control System

A combination of active and passive thermal controls is implemented to minimize parasitic heat leak into the TAs to maximize the AC loss portion of the calorimetric wattage. Passive thermal controls are used to minimize the tare parasitic heat leak into the TA and to maintain core rig external surface temperatures above freezing. The active thermal controls minimize the tare heat leak into the TA, maintaining components in a suitable operating temperature range, and are used for posttest rapid warming. There is no active thermal control hardware in the vacuum gap besides the TA itself.

All surfaces that can be seen by the TA are treated in some fashion to reduce the radiation heat leak portion of the tare. First, the rotor stainless steel outer surface is highly polished to reduce emissivity to 0.16 (room temperature value). As mentioned previously, the back iron is cooled to 80 K and has an emissivity of

0.95, but the back iron plenum wall and back iron support are both covered in aluminized Mylar® (DuPont Teijin Films). All other internal surfaces seen by the TAs have a single layer of aluminized Mylar® attached with an emissivity of 0.05. All surfaces except the TAs use regular Mylar® while the TA has striated Mylar® due to the presence of the magnetic field and potential for large eddy currents; striated Mylar® essentially breaks a single large conducting Mylar® piece into numerous small squared sections. To reduce the conduction heat leak into the TAs, contact areas are minimized. Appendix B shows that less than 2 W of parasitic heat leaks into the TA.

For active thermal control, heaters are applied to the bearings, vessel lid, nitrogen vent, and TA power leads to maintain temperature above ambient as needed during operation. Thermal modeling showed that some of these surfaces dropped below ambient (in some cases below the freezing point of water) during normal testing. Heaters will not exceed 80 percent of the autoignition temperature of hydrogen, per 501.135 (B) (1) (1) of the NFPA 70 National Electric Code (NEC). Further details on the thermal modeling are in Appendix B.

6.0 Power System

The purpose of the power system is to provide the necessary current, voltage, waveform, and frequency for the TAs. The power system consists of the hardware and cabling needed to control and inject AC current (and DC) into any TA inside the core rig and control DC power to the calorimetry calibration test article. Thus, two separate power supplies are employed. The power supplies are located in the shop area in SMiRF, and thus configured to run remotely.

6.1 Test Article Power Supply (TAPS)

The TAPS characteristics are as follows:

- $0 < I_T < 400$ A DC or peak AC
- AC frequency range 1 Hz $< f <$ 400 Hz
- AC phase angle $-180° < \phi < 180°$
- Any input AC waveform for I_T
- Any ramp up or down rate for I_T
- Slew-rate limited I_T of 1 MA/s
- <0.2-percent rms harmonic distortion
- Remote switching between (up to) four TAs
- Single-phase output

The TAPS is a controlled current source, coupled to the TA through an inductor, where $d\left(I_{TA}\right)/dt = \left(V_{TAPS} - V_{TA}\right)/L$, and I_{TA} is test article current, L is inductance, t is time, V_{TA} is test article voltage, and V_{TAPS} is test article power source voltage. The inductor provides low-pass filtering of the pulse width modulation (PWM) switching in the TAPS voltage source.

The power is equal to and opposite that of the rotor drive motor to provide torque balance and constant speed. DC links are connected between the rotor driver inverter and the TAPS amplifier, allowing power to recirculate outside of the utility-side interface. This is depicted in Figure 19 for phase angles within and beyond ±90°. This mode of operation simplifies the rectifiers for both TAPS and rotor driver inverter.

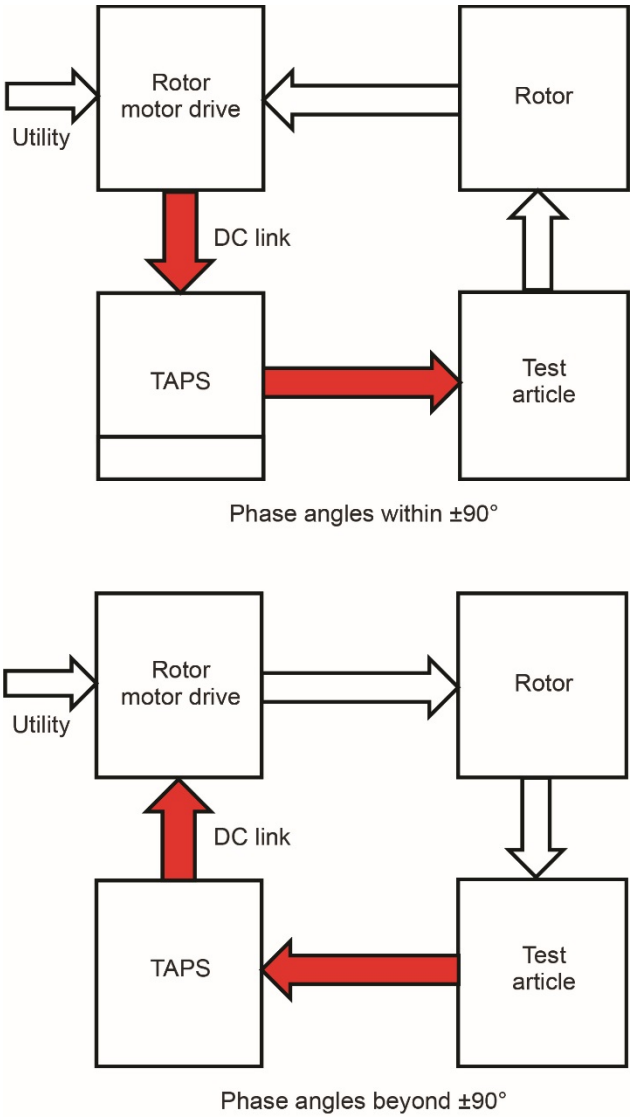

Figure 19.—Test article power supply (TAPS) power flow diagram, where DC is direct current.

The TAPS block diagram is shown in Figure 20. Commands are sent to the main controller, which sends signals to the power amplifier. Communication between the rotor drive VFD ensures matching frequencies as discussed. The amplifier then powers one of the four TAs with feedback control.

The amplifier is a high-power four-quadrant transconductance switch-mode amplifier with the ability to generate any arbitrary current waveform based on voltage command input. It has an internal current control loop with a variable transconductance gain and output offset. As shown in Figure 20, there is a tunable analog control circuit to accommodate different loads. The amplifier also has remote shutdown and DC supply overvoltage and undervoltage protection.

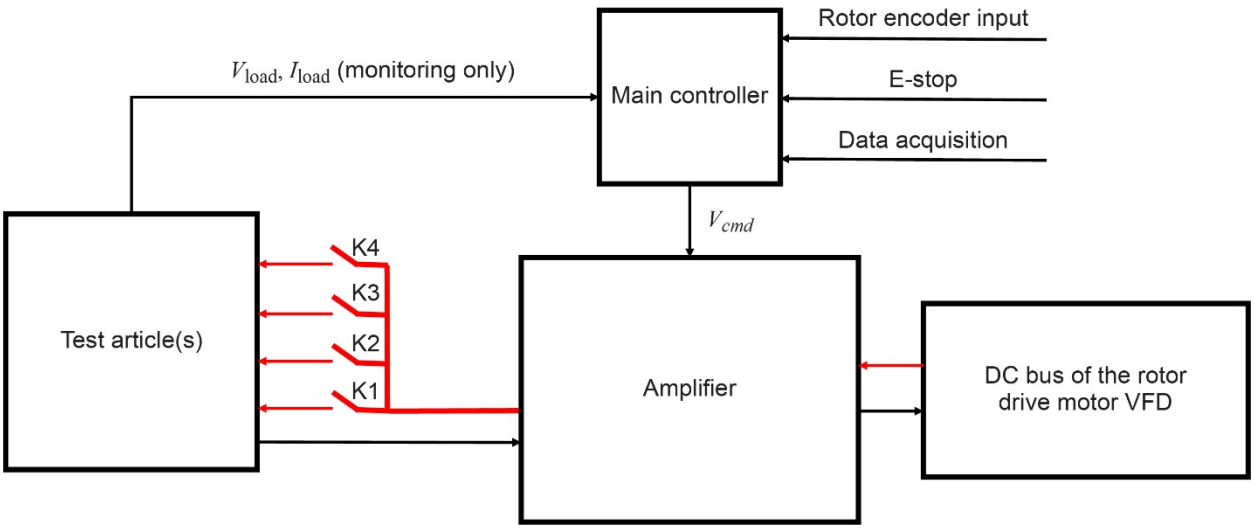

Figure 20.—Test article power supply block diagram, where DC is direct current, I_{load} is load current, V_{cmd} is command voltage, V_{load} is load voltage, and VFD is variable frequency drive.

6.2 Calorimetry Calibration Power Supply (CCPS)

The CCPS characteristics are shown below:

- Up to 80 W of DC power is provided to a known resistive heater
- Remote switching between (up to) four TAs

CCPS is a DC power supply with analog control input with either constant current or constant voltage mode. The heater resistor voltage is sensed through the same channels used for the TA voltage for a Kelvin connection.

7.0 Fluids System

The fluids system consists of anything that stores, controls, or provides fluids necessary for testbed operation. The primary purpose of the fluids system is to supply coolant to the TAs with the following characteristics:

(1) Single-phase LH_2 through the TA
(2) TA coolant inlet temperature of 18 K < $T \leq$ 24 K
(3) TA coolant inlet pressure of 135 kPa < $P \leq$ 618 kPa
(4) TA flow rate 0.05 g/s < $\dot{m} \leq$ 2.0 g/s (for one TA)

Other secondary characteristics of the fluids system are as follows:

(5) To supply LH_2 at $T \leq$ 24 K to all TA interfaces
(6) To supply LN_2 to maintain the back iron plenum at $T \leq$ 80 K, exclusive of the rotor temperature
(7) To provide purging and venting capability for all fluid transport lines (GHe or GN_2).
(8) To provide leak check capability (GHe)
(9) To provide vacuum to the test rig to minimize windage and tare parasitic heat leak into the TAs

Figure 21 depicts the basic TA process stream. Figure 22 shows the process and instrumentation diagram (P&ID). LH_2 flows from a large roadable dewar parked outside SMiRF. The fluid starts in a saturated state near ambient pressure. All lines outside the core test rig are vacuum jacketed (VJ). The fluid is pressurized in the roadable dewar. Then fluid is routed through a cryogenic refrigerator, otherwise known as a cryocooler heat exchanger. A dual-stage cooling system is used to remove up to 80 W at 20 K from the fluid using high-purity copper cylinders with a very high residual resistance ratio (RRR) value attached to the cold head. The heat exchanger can cool the fluid near the triple line. The coolers and cylinders are enclosed inside a VJ dewar. Next, the fluid is routed through a heater system that is used to precisely adjust the thermodynamic state of the fluid to the inlet of the TA. Fluid then flows into the core rig and through the TA. TA inlet and exit pressures are monitored to adjust both the cooler and the heater power. Finally, fluid is routed out of the core rig, through a bank of mass flowmeters, and then to vent out of the facility. Temperature is controlled through control of the cryocooler and heater. Pressure is controlled upstream in the roadable dewar. The flow rate is controlled through control of the up and downstream pressures.

In terms of operation, for simplicity, it is desired to maintain a constant temperature difference across the TA. To do so, the inlet state of the fluid is first set through control of the cryocooler and the heater. The rotor and/or injection current is operated, generating some AC loss. Since AC losses will vary with operation, the flow rate is adjusted accordingly to increase or decrease the exit temperature. Changing the flow rate would also then change the inlet condition, so the heater, cryocooler controls, and flow rate are all adjusted for a given AC loss value in order to achieve steady-state constant temperature difference across the TA.

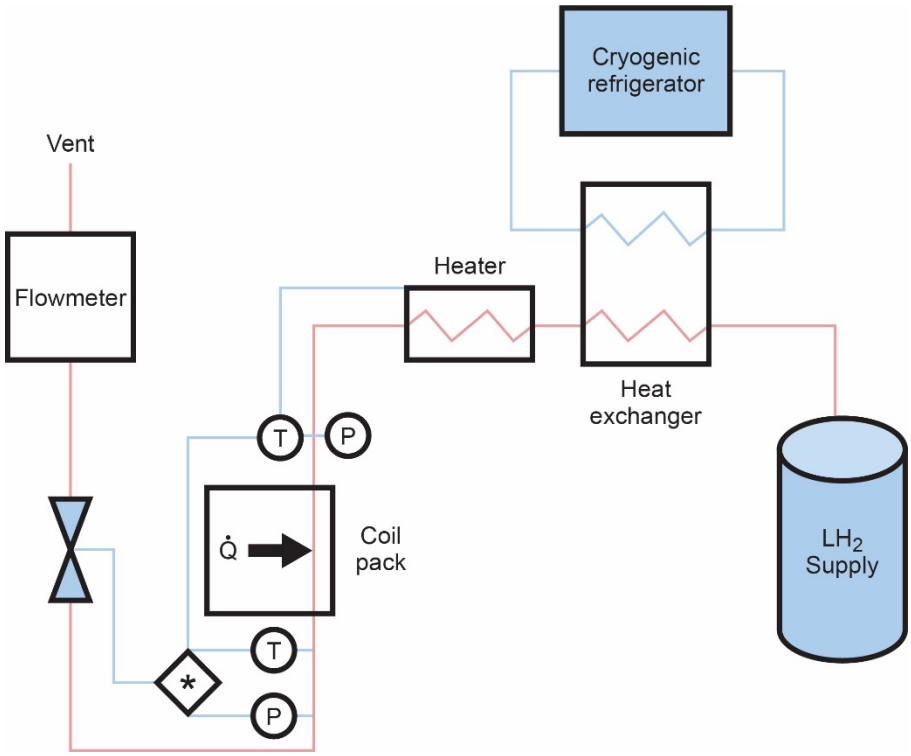

Figure 21.—Test article process stream.

Pressure drop across TAs is expected to be low due to the low dynamic viscosity of hydrogen. For example, flow modeling shows that the expected single-phase LH_2 pressure drop across the TA flow channel shown in Figure 5 is <6.9 kPa (<1 psi). This low-pressure drop is due to the fact that nearly all of the pressure drop occurs across the backpressure control valve. Precise backpressure control is provided through the SMiRF flow control system. Flashing will occur across the valve, but noise is predicted to be low due to the low average fluid velocity.

Meanwhile, LN_2 is used to fill the plenum section behind the back iron. The plenum is maintained at 203 kPa (30 psi). As the back iron heats, LN_2 boils off to vent. Periodically, the liquid level is replenished during testing.

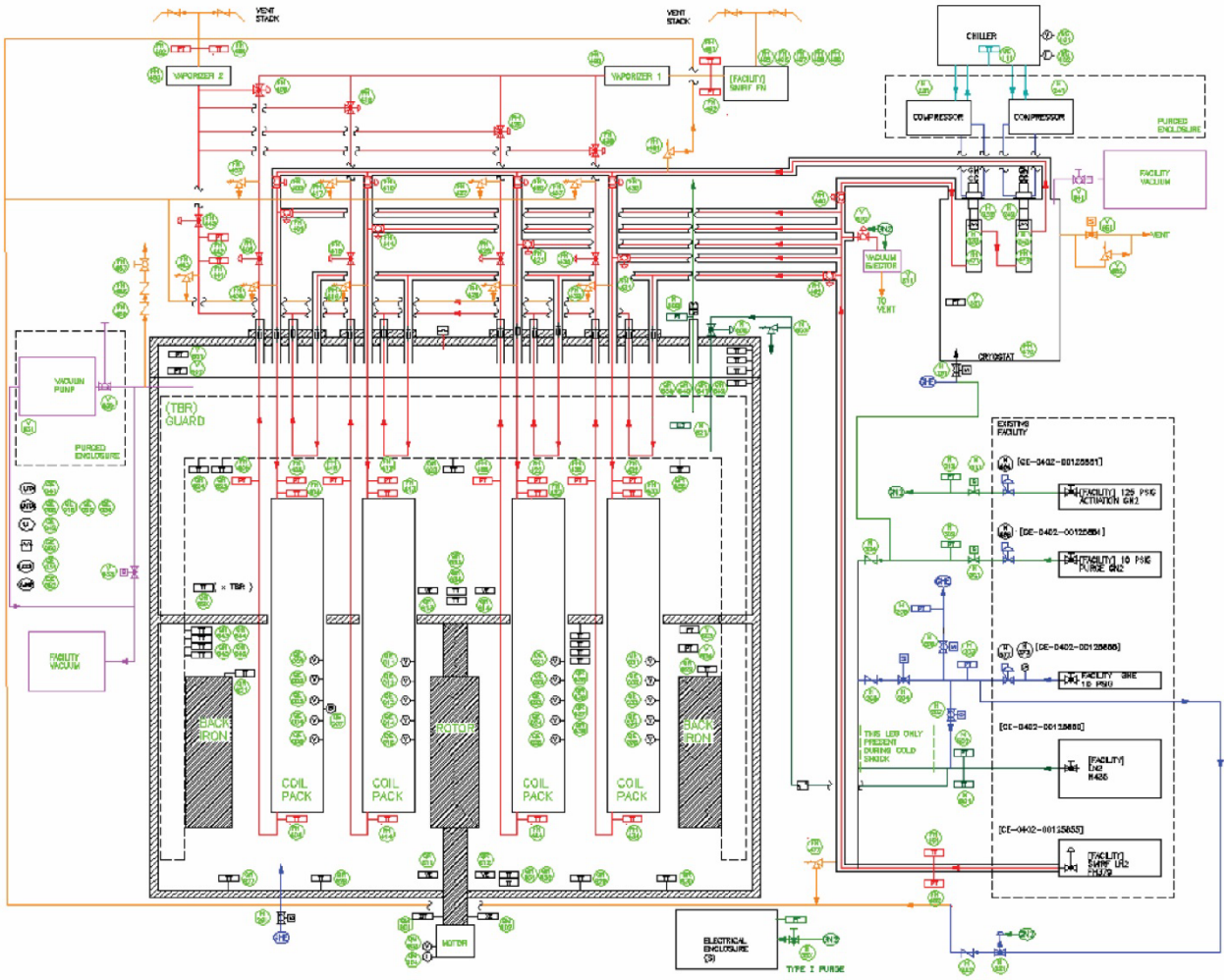

Figure 22.—Process and instrumentation diagram.

8.0 Instrumentation and Data Acquisition (DAQ)

The purpose of the instrumentation and DAQ systems is to make measurements, record and collect data, and monitor and provide feedback to the control system. The instrumentation and DAQ systems consist of all the sensors, devices, conditioners, and cabling required to meet this purpose. Measurements fall into two categories:

(1) Science
(2) Health and status

Some of these measurements serve both of these purposes. All instruments were chosen based on the ability to function properly within the operational environment corresponding to the location.

The instrumentation and DAQ signal conditioning equipment is located in the SMiRF shop area, as shown in Figure 9. All instrument data is sent to the testbed main controller. Some instrument data is also sent to stand-alone controllers like the power supplies and the rotor motor speed controller. The primary science measurement is the TA superconductor AC losses that are determined via flow calorimetry, which are based on temperatures, pressures, and flow rate measurements.

An overview of the sensors used throughout the testbed are given below; details subsequently follow.

(1) Temperature
    (a) Inside magnetic field, <77 K: Cernox® sensors
    (b) Outside magnetic field, <77 K: silicon diodes
    (c) Outside magnetic field, >77 K: thermocouples
(2) Pressure
    (a) Pressure throughout the flow system: standard pressure transducers
    (b) Inlet and outlet TA fluid pressure: high-accuracy pressure transducers
    (c) Vacuum pressure: cold cathode ion gauge rated for gaseous hydrogen exposure
(3) Liquid level in the LN_2 plenum: cryogenic rated capacitance probe
(4) Mass flow rate: standard gas flowmeters with overlapping ranges
(5) Acceleration: noncryogenic rated standard sensors
(6) Proximity: angular position indicator
(7) Magnetic field: Hall sensors
(8) Current: standard transducers
(9) AC voltage: voltage attenuators and isolation amplifiers
(10) DC voltage: nanovoltmeter

8.1 Test Article (TA) Sensors

Table 2 to Table 6 show the details of all the sensors used for the various TAs, which includes calibration TAs as well as normal TAs. As shown, both inlet and exit thermodynamic states of the fluid are measured in situ inside the core rig; flow rate, current, and voltage are taken outside of the vessel. Note from Figure 23 that these inlet and exit temperature readings are true stream readings, not outer wall measurements. Note also that the effect of heat addition from the pressure transducer sensor body into the fluid on the calorimetry measurements is nulled by placing the pressure measurement before the temperature measurement.

TABLE 2.—CALORIMETRY CALIBRATION TEST ARTICLE INSTRUMENTATION

Scan rate	Name	Purpose	Location	Justification	Range	Uncertainty, U
1 Hz	Ttasx	Health, science	Mounted on outside of dummy coil pack, side facing rotor	Measure surface temperature of coil pack during checkouts	4 to 325 K	±9 mK at 20 K; ±36 mK at 300 K
1 Hz	Ttasx	Health, science	Mounted on outside of dummy coil pack, side facing back iron	Measure surface temperature of coil pack during checkouts	4 to 325 K	±9 mK at 20 K; ±36 mK at 300 K
1 Hz	I_{ch}[a]	Health, science	Heater power leads outside dewar	Measure calibration heater current	0 to 4 A needed, device is ±30 A measured range	±1 percent FS[b]
1 Hz	V_{ch}[c]	Health, science	Mounted on leads immediately downstream of heater power lead joint	Measure calibration heater voltage	0 to 100 V in (0 to 20 V needed)	±0.1 V (nonlinearity and offsets)
1 kHz	B_{TA}[d]	Health, science	On coil outer surface	Monitor magnetic field on single sample	0 to 5 T	Sum of 1. U in raw peak magnetic field, B, measurement 2. U in control current 3. U in voltage readout (2 to 6 percent)

[a]Calibration heater current.
[b]Full scale.
[c]Calibration heater voltage.
[d]Test article magnetic field.

TABLE 3.—TEST ARTICLE (TA) INSTRUMENTATION AT INLET

Scan rate	Name	Purpose	Location	Justification	Range	Uncertainty, U
1 kHz	P_{CS}[a]	Health, science	Inlet line to TA	1. Calorimetry 2. Along with T_{CS},[b] determine thermodynamic state of the fluid (hydrogen, nitrogen) during all phases of testing 3. Derive parasitic heat leak 4. Derive AC[c] losses (flow, spin, power) 5. Perform calibration tare heat leak 6. Used to measure pressure drop across TA	0 to 1.034 MPa (0 to 150 psia)	±1.8 percent FS[d]
1 Hz	T_{CS}[d]	Health, science	Inlet line to TA	1. Calorimetry 2. Along with P_{CS}, determine thermodynamic state of the fluid (hydrogen, nitrogen) during all phases of testing 3. Derive parasitic heat leak 4. Derive AC losses (flow, spin, power) 5. Perform calibration tare heat leak	4 to 325 K	±9 mK at 20 K; ±36 mK at 300 K

[a]Coolant supply pressure.
[b]Coolant supply temperature.
[c]Alternating current.
[d]Full scale.

TABLE 4.—TEST ARTICLE (TA) INSTRUMENTATION AT EXIT

Scan rate	Name	Purpose	Location	Justification	Range	Uncertainty, U
1 Hz	P_{CE}[a]	Health, science	Exit line to TA	1. Calorimetry 2. Along with T_{CE},[b] determine thermodynamic state of the fluid (hydrogen and nitrogen) during all phases of testing 3. Derive parasitic heat leak 4. Derive AC[c] losses (flow, spin, and power) 5. Perform calibration tare heat leak 6. Used to measure pressure drop across TA	0 to 1.034 MPa (0 to 150 psia)	±1.8 percent FS[d]
1 Hz	T_{CE}	Health, science	Exit line to TA	1. Calorimetry 2. Along with P_{CE}, determine thermodynamic state of the fluid (hydrogen and nitrogen) during all phases of testing 3. Derive parasitic heat leak 4. Derive AC losses (flow, spin, and power) 5. Perform calibration tare heat leak	4 to 325 K	±9 mK at 20 K; ±36 mK at 300 K

[a]Coolant exit pressure.
[b]Coolant exit temperature.
[c]Alternating current.
[d]Full scale.

TABLE 5.—TEST ARTICLE INSTRUMENTATION FOR MEASURING FLOW FOR CALORIMETRY

Scan rate	Name	Purpose	Location	Justification	Range	Uncertainty, U
1 Hz	$\dot{m}$[a]	Health, science	Vent line, downstream of vaporizer 1	1. Determine flow rate to measure flow energy for calorimetry	0 to 0.05 stdL/min	±0.5 percent reading ±0.2 percent FS[b]
1 Hz	$\dot{m}$	Health, science	Vent line, downstream of vaporizer 1	1. Determine flow rate to measure flow energy for calorimetry	0 to 0.1 stdL/min	±0.5 percent reading ±0.2 percent FS
1 Hz	$\dot{m}$	Health, science	Vent line, downstream of vaporizer 1	1. Determine flow rate to measure flow energy for calorimetry	0 to 0.5 stdL/min	±0.5 percent reading ±0.2 percent FS
1 Hz	$\dot{m}$	Health, science	Vent line, downstream of vaporizer 1	1. Determine flow rate to measure flow energy for calorimetry	0 to 1, 2 stdL/min	±0.5 percent reading ±0.2 percent FS

[a]Mass flow rate.
[b]Full scale.

TABLE 6.—TEST ARTICLE (TA) INSTRUMENTATION FOR MEASURING VOLTAGE AND CURRENT

Scan rate	Name	Purpose	Location	Justification	Range	Uncertainty, U
1 Hz	V_{TA}[a]	Health, science	Coil taps	1. Measure low voltage for DC[b] tests prior to and after AC[c] tests 2. Measure AC voltage across superconductor or a copper solder joint	±600-V input	2 to 4 percent
1 Hz	I_{ITA}[d]	Science, health	Coil power lead outside dewar	1. Measure injected transport current into TA during all phases of testing	±400-A measured range; device range is 0 to 600-A peak, 0 to 100-A rms	±1 percent FS[e]

[a]TA voltage.
[b]Direct current.
[c]Alternating current.
[d]TA injected current.
[e]Full scale.

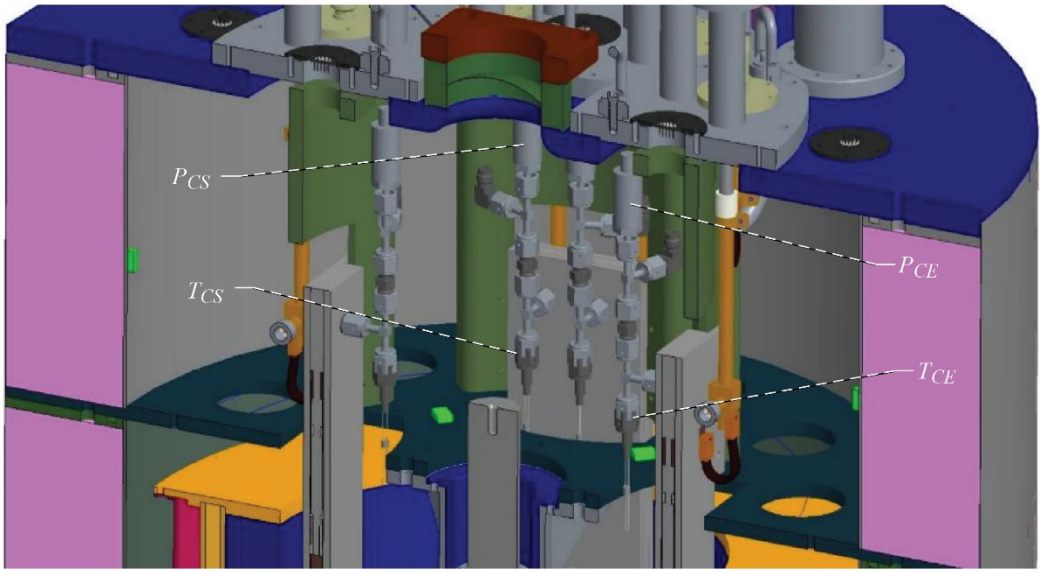

Figure 23.—Location of pressure and temperature measurements for calorimetry, where P_{CE} is coolant exit pressure, P_{CS} is coolant supply pressure, T_{CE} is coolant exit temperature, and T_{CS} is coolant supply temperature.

8.2 Core Test Rig Sensors

Table 7 and Table 8 outline the sensors used in the core test rig. Figure 24 shows where some of these measurements are physically located within the rig. Temperature sensors in the main portion of the core rig are for monitoring changes in the tare parasitic heat leak induced during operation (e.g., a warmer rotor surface as it spins for extended time periods, small changes in the back iron wall temperature due to fluctuating LN_2 bath pressure, etc.). Thermocouples are mounted on the top and middle portions of the core rig primarily for health. Sensors mounted on the outside of the lid are for monitoring temperature to determine when to engage the heaters. Thermocouples mounted on the vessel bottom are used for a similar purpose, along with leak detection. Meanwhile accelerometers are mounted to monitor rotor imbalance, modal excitation, and bearing integrity.

TABLE 7.—CORE RIG INSTRUMENTATION I

Scan rate	Name	Purpose	Location	Justification	Range	Uncertainty, U
50 Hz	P_{vv}	Health	Top of vessel; bottom of vessel	Monitor pressure level inside annular space that surrounds test articles during all phases Redundancy	1×10^{-9} to 1,500 torr	5×10^{-8} to 100 mtorr: ±30 percent of reading; 100 mtorr to 50 torr: ±5 percent of reading; 50 to 1,000 torr: ±1 percent of reading
1 Hz	A_B[a]	Health	At lower bearing, axis toward shaft (horizontal) At lower bearing, 90° from other accelerometers	1. Monitor rotor imbalance 2. Monitor modal excitation 3. Monitor bearing integrity	0 to 75g	±5 percent; $1<f<20$ kHz; 233 to 394 K
1 Hz	A_B	Health	At upper bearing, axis toward shaft (horizontal) At upper bearing, 90° from other accelerometers	1. Monitor rotor imbalance 2. Monitor modal excitation 3. Monitor bearing integrity	0 to 75g	±5 percent; $1<f<20$ kHz; 233 to 394 K

[a]Acceleration, m/s²

TABLE 8.—CORE RIG INSTRUMENTATION II

Scan rate	Name	Purpose	Location	Justification	Range	Uncertainty, U
1 Hz	T_{sx}[a]	Health, science	Back iron	Monitor temperature of back iron during all phases of testing	4 to 325 K	±9 mK at 20 K ±36 mK at 300 K
1 Hz	T_{sx}	Health, science	Outside vacuum chamber, top, bottom 12 times	Monitor temperature of top, bottom of vacuum chamber	73 to 1,173 K	For T < 273 K, greater of 1.7 K or 1.0 percent For T > 273 K, greater of 1.7 K or 0.5 percent
1 Hz	T_{sx}	Health	Upper chamber top, bottom 8 times	Monitor temperature of top, bottom of upper chamber	73 to 1,173 K	For T < 273 K, greater of 1.7 K or 1.0 percent For T > 273 K, greater of 1.7 K or 0.5 percent
1 Hz	T_{sx}	Health	Middle plate 8 times	Monitor temperature of the middle plate	73 to 1,173 K	For T < 273 K, greater of 1.7 K or 1.0 percent For T > 273 K, greater of 1.7 K or 0.5 percent
3 kHz	I_{ITA}[b]	Health, science	Mounted near test article (TA) power supply	Measure injected transport current into TA coil pack	0 to 400 A	1 percent

[a]Surface temperature.
[b]Test article injected current.

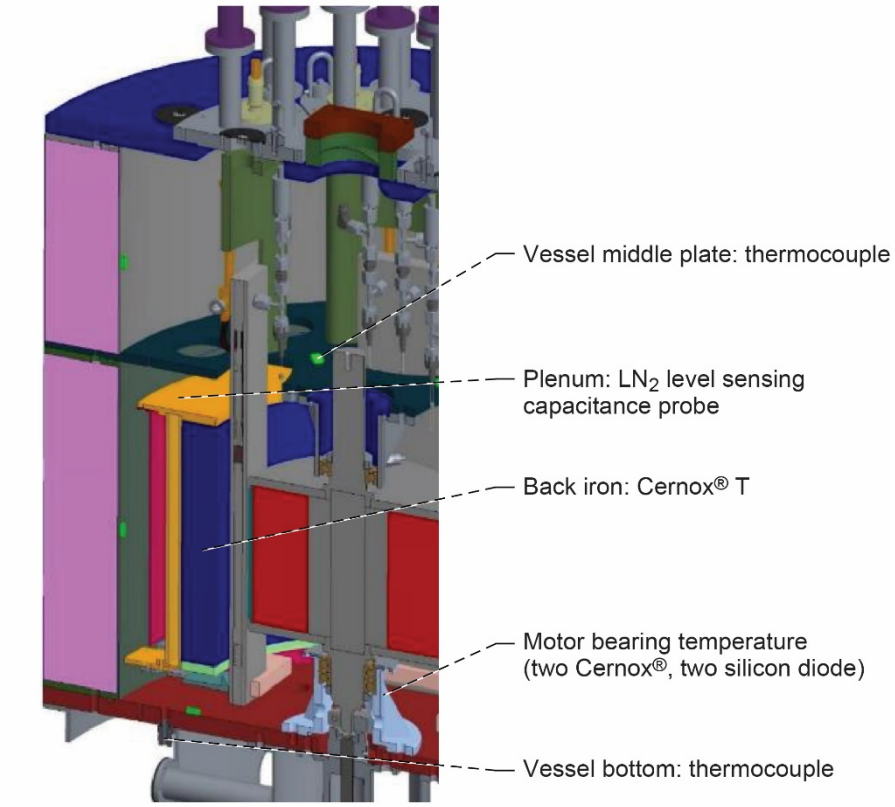

Figure 24.—Location of several sensors inside core rig.

8.3 Rotor Drive Sensors

Table 9 outlines sensors used for the rotor drive system. Both proximity and speed of the rotor are measured as well as the power into the motor. The temperature of the top and bottom bearing housing is also measured using high-accuracy sensors due to the likelihood of rotor temperature changes during operation. Coupled with heater operation, the high-accuracy temperature sensors eliminate the need to optically measure the rotor temperature surface in situ inside the vacuum annular space inside the core rig. The heaters, along with tight feedback control, ensure that the rotor surface temperature does not vary significantly, ensuring that the tare parasitic heat leak value does not change significantly as operation conditions vary.

8.4 Fluid System Instrumentation

Instrumentation is placed throughout the fluid system primarily for health monitoring. Wherever possible, standard grade pressure transducers and thermocouples and silicon diodes are implemented. Below is a summary of the sensors:

(1) Pressure and stream temperature to monitor the thermodynamic state of the LH_2 from the roadable dewar.

(2) Pressure and stream temperature to monitor the thermodynamic state of the LN_2 from the roadable dewar.
(3) Pressure and stream temperature to monitor the thermodynamic state of the LH_2 to cool the power leads.
(4) Pressure and skin temperature to monitor the thermodynamic state of the fluid downstream of the SMiRF heat exchanger to vent.
(5) Pressure and stream temperature to monitor the thermodynamic state of the hydrogen to infer density to convert volumetric flow rate into mass flow rate.
(6) Skin temperature on the vent lines to ensure no venting of liquid.
(7) Pressure transducers throughout to monitor valve actuation for pressurizing and purging.
(8) Cryocooler, temperature of the water used to chill the unit.
(9) Cryocooler, current and voltage to determine the cooler power.
(10) Cryocooler, vacuum pressure to monitor pressure of cryocooler dewar.
(11) Cryocooler, pressure to monitor GHe line.

TABLE 9.—ROTOR DRIVER INSTRUMENTATION

Scan rate	Name	Purpose	Location	Justification	Range	Uncertainty, U
1 kHz	q_R[a]	Science, health	Back end of motor shaft	1. Clock the rotor during DC[b] testing (to have max. or min. field facing coil) 2. Angular position indicator	0 to 6,000 rpm	0.176°
1 Hz	ω_r[c]	Science, health	Perpendicular to driver motor shaft, <1.25 cm away	Measure rotor speed for all phases of operation	1 to 1×10^6 rpm, 233 to 458 K	Worse of ±1 rpm or 0.005 percent FS[d] from tachometer
1 kHz	V_{rd}[e]	Health	Integral to drive motor	Monitor voltage to driver motor	0 to 200 V	~1 percent
1 kHz	I_{rd}[f]	Health	Integral to drive motor	Monitor current to driver motor	0 to 81 A	~1 percent
1 Hz	T_b[g]	Health, science	Mounted on rotor bearing housing 2 times	1. Measure rotor bearing temperature 2. Infer temperature of rotor inside chamber	4 to 325 K	±9 mK at 20 K ±36 mK at 300 K
1 Hz	T_b	Health, science	Mounted on rotor bearing housing 2 times	1. Measure rotor bearing temperature 2. Infer temperature of rotor inside chamber 3. Redundancy	1.4 to 500 K	±1 K

[a]Motor rotation.
[b]Direct current.
[c]Rotor speed.
[d]Full scale.
[e]Driver motor voltage.
[f]Driver motor current.
[g]Bearing temperature.

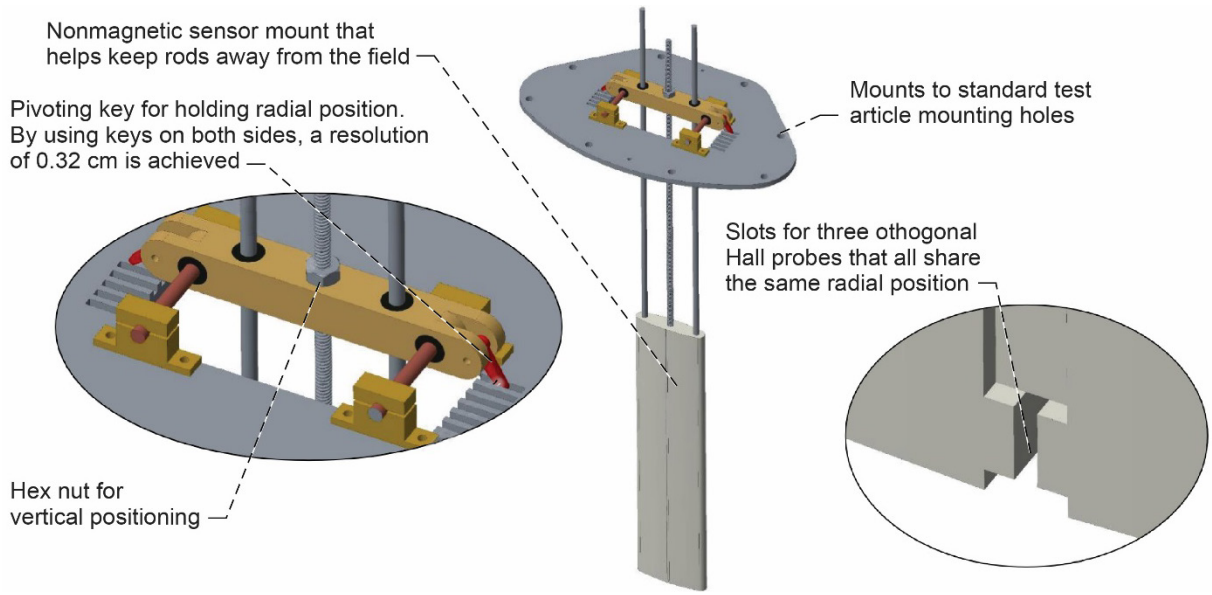

Figure 25.—Magnetometer probe illustration.

8.5 Magnetometer

Prior to testing, a custom-built three-axis magnetometer can be used to map the radial component of the magnetic field inside the core rig. Features of the magnetometer are shown in Figure 25. The measurement is also intended to validate magnetic field models and to verify the electromagnetic field is working properly. The uncertainty in magnetic field measurement is a function of excitation current, but is generally below 3 percent at nominal operating conditions.

8.6 Data Acquisition (DAQ)

The DAQ system consists of all of the components necessary to interface between the sensors and the computer used to store data. Working with a hazardous fluid requires remote operation and forces all data to be sent to a remote control and monitoring station via Ethernet cables. High current and voltage and low current and voltage measurements are separated to protect against unwanted noise. Signal conditioners are used wherever possible to ensure high signal levels (e.g., nanovoltmeter for DC superconducting tests). Whenever in close proximity to the magnetic field, each four-wire device is quad-twisted to prevent eddy currents and/or unwanted offsets in the output signals. Low-noise feedthroughs and cables are used to transmit signals through the lid. Both low- and high-speed DAQ cards are implemented.

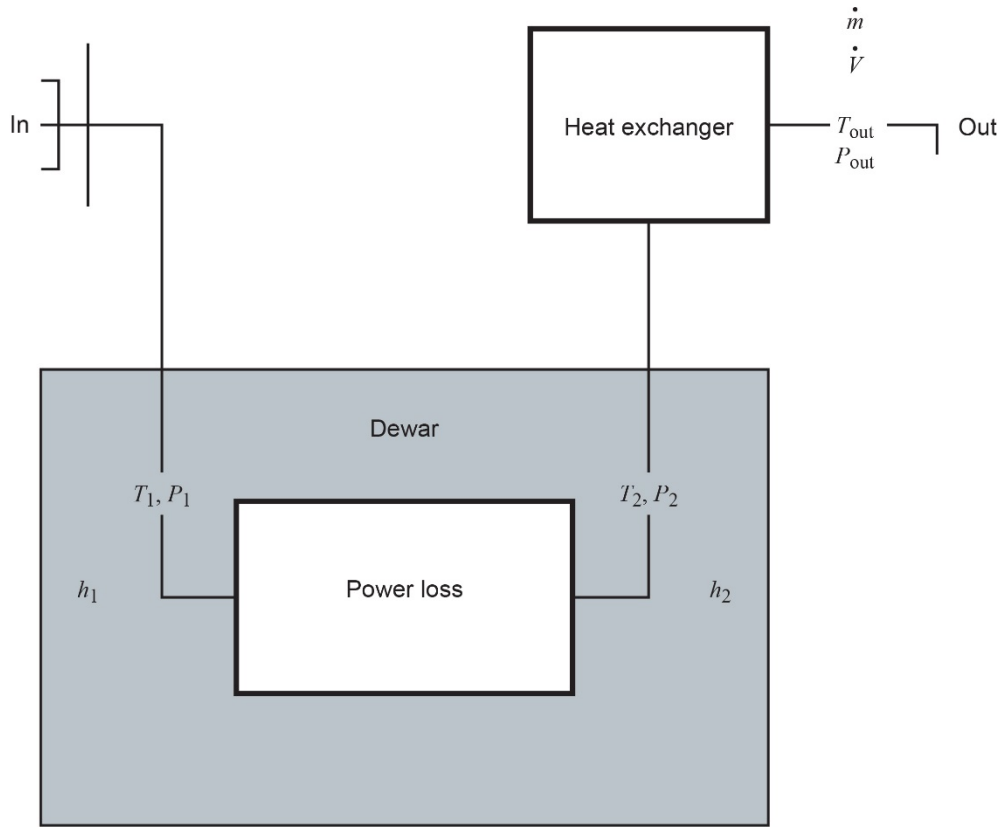

Figure 26.—Sensors used in uncertainty analysis, where h_1 is enthalpy 1, h_2 is enthalpy 2, $\dot{m}$ is mass flow rate, P_{out} is output pressure, T_{out} is output temperature, and $\dot{V}$ is volumetric flow rate.

8.7 Calorimetry Uncertainty Analysis

The primary measurement is the AC loss measurement, which is directly inferred from the flow calorimetry measurement. Uncertainty analysis was conducted to optimize selection of the sensors involved in the measurement, as well as to minimize uncertainty in the measurement. Figure 26 illustrates the sensors involved in the calculation, including TA inlet temperature and pressure, outlet temperature and pressure, and volumetric flow rate. Note that an additional two sensors and an equation of state (EOS) are required to determine density and to turn the volumetric flow rate into a mass flow rate.

Assumptions required to do the uncertainty analysis are as follows:

(1) The outlet condition is maintained at 101 kPa (14.6 psi) and 297 K, which is chosen as a worst-case scenario to maximize uncertainty at the flowmeter reading. In reality, the pressure will be slightly higher.
(2) There is no correlation between flow rate and density or enthalpy. This maximizes uncertainty versus choosing that the values are correlated.

The flow calorimetry equation is

$$\dot{Q} = \dot{m}\left(h_2 - h_1\right) \tag{6}$$

where $\dot{m}$ is mass flow rate, h is enthalpy, and $\dot{Q}$ is heat rate.

Substituting using the sensor names in Figure 26:

$$\dot{Q} = \dot{V}\rho\left(P_{\text{out}}, T_{\text{out}}\right)\left[h_2\left(P_2, T_2\right) - h_1\left(P_1, T_1\right)\right] \tag{7}$$

where P_{out} is output pressure, T_{out} is output temperature, and $\dot{V}$ is volumetric flow rate.

Density, ρ, and enthalpy are determined using the REFPROP EOS (Ref. 6). The uncertainty in density is

$$U_\rho = \sqrt{\left(\frac{d\rho}{dP}\right)^2 U_{P_{\text{out}}}^2 + \left(\frac{d\rho}{dT}\right)^2 U_{T_{\text{out}}}^2 + 2\frac{d\rho}{dP}\frac{d\rho}{dT}U_{P_{\text{out}}}U_{T_{\text{out}}}\delta_{PT}} \tag{8}$$

where P is pressure and T is temperature.

The uncertainties in mass flow rate and enthalpy are as follows, respectively:

$$U_{\dot{m}} = \sqrt{\left(\dot{V}\right)^2 U_\rho^2 + \rho^2 U_{\dot{V}}^2} \tag{9}$$

$$U_h = \sqrt{C_p{}^2 U_T^2 + \left(\frac{dh}{dP}\right)^2 U_P^2 + 2C_p\frac{dh}{dP}U_T U_P \delta_{PT}} \tag{10}$$

where C_P is specific heat.

For purposes of determining the actual AC losses as a function of operating conditions (f, B), the calorimetry heat leak value must be corrected for the tare heat leak value taken at a state where there is no current flowing and the rotor is not spinning. This ensures that the calorimetry value is purely from parasitics. Thus, the corrected expression to determine AC losses becomes

$$\dot{Q}_{AC}\left(f, B\right) = \dot{m}\left[h_2 - h_1\right] - \dot{Q}_{tare} \tag{11}$$

Note that if any of the surfaces in direct line of sight with the TA warmup or cooldown during operation, then the rig must be returned to a no-spin, no-current state and the tare value determined again. This method of operation may limit test runs to a short duration, but it minimizes drift in the parasitic tare value.

Uncertainty analysis was performed over the entire operating envelop using the known uncertainty values in each of the seven sensors. Table 10 lists results. As shown, the minimum, maximum, and average expected uncertainty over the operating envelop are 1.63, 3.01, and 2.46 percent, respectively, for a single flow calorimetry value. Therefore, the resultant uncertainty in the AC loss measurement will be twice these values, for an average total uncertainty of ~5 percent. As expected, the uncertainty is dominated by temperature and not by pressure.

9.0 Control System

The purpose of the control system is fourfold:

(1) To send commands
(2) To receive, process, and display testbed data
(3) To access testbed historical operational data to compare and display
(4) To safe the testbed when the limits of critical conditions have been reached and immediate action must be taken

TABLE 10.—UNCERTAINTY ANALYSIS

Measured quantities					Uncertainties, U							Power, $\dot{Q}$, and uncertainty. U	
T_1, K	T_2, K	P_1, kPa	P_2, kPa	$\dot{m}$, g/s	U_{T1}, percent	U_{T2}, percent	U_{P1}, percent	U_{P2}, percent	$U_{\dot{V}}$, percent	$U_{T\text{out}}$, percent	$U_{P\text{out}}$, percent	$\dot{Q}$, W	U, percent
18	20	145	138	0.04	0.05	0.05	12.86	13.5	0.01	0.33	0.5	0.83	2.95
18	20	407	400	.04	.05	.05	4.58	4.66	.01	.33	.5	.82	2.99
24	26	407	400	.04	.04	.03	4.58	4.66	.01	.33	.5	1.22	1.63
18	20	614	607	.04	.05	.05	3.02	3.05	.01	.33	.5	0.82	3.01
24	26	614	607	.04	.04	.03	3.02	3.05	.01	.33	.5	1.19	1.73
18	20	145	138	.53	.05	.05	12.86	13.5	.01	.33	.5	9.98	2.95
18	20	407	400	.53	.05	.05	4.58	4.66	.01	.33	.5	9.88	2.99
24	26	407	400	.53	.04	.03	4.58	4.66	.01	.33	.5	14.63	1.63
18	20	614	607	.53	.05	.05	3.02	3.05	.01	.33	.5	9.8	3.01
24	26	614	607	.53	.04	.03	3.02	3.05	.01	.33	.5	14.26	1.73
18	20	145	138	1.06	.05	.05	12.86	13.5	.01	.33	.5	19.97	2.95
18	20	407	400	1.06	.05	.05	4.58	4.66	.01	.33	.5	19.76	2.99
24	26	407	400	1.06	.04	.03	4.58	4.66	.01	.33	.5	29.26	1.63
18	20	614	607	1.06	.05	.05	3.02	3.05	.01	.33	.5	19.6	3.01
24	26	614	607	1.06	.04	.03	3.02	3.05	.01	.33	.5	28.52	1.73
18	20	145	138	1.95	.05	.05	12.86	13.5	.01	.33	.5	36.6	2.95
18	20	407	400	1.95	.05	.05	4.58	4.66	.01	.33	.5	36.22	2.99
24	26	407	400	1.95	.04	.03	4.58	4.66	.01	.33	.5	53.64	1.63
18	20	614	607	1.95	.05	.05	3.02	3.05	.01	.33	.5	35.94	3.01
24	26	614	607	1.95	.04	.03	3.02	3.05	.01	.33	.5	52.29	1.73
				Average	.05	.04	5.61	5.78	.01	.33	.5	-------	2.46

This system is responsible for controlling

(1) TAPS
(2) Rotor drive motor
(3) Heaters
(4) Fluid system valves
(5) Cryocooler LH_2 temperature

Control system algorithms are developed to operate the test rig in any of the seven operating modes discussed in Appendix E. A timer is used to ensure the controller is operating properly and communicating with the control room.

The control system consists of the hardware and software necessary to safely operate the test rig. The testbed control system comprises a computer, graphical user interface (GUI), and the main testbed controller. The computer and GUI are situated remotely from the testbed in the SMiRF control room, while the main testbed controller is located in the shop area of the SMiRF test facility shown in Figure 9. The computer runs the GUI software, stores testbed data, communicates with both the testbed main controller and SMiRF controller, and keeps track of TAs.

DSpace is chosen for the control software. It features a gigabit Ethernet host interface, all the necessary input and outputs, a flexible interface with other control systems (SMiRF and DAQ), and a completely customizable GUI. The control system architecture is shown in Figure 27.

The computer timestamps and stores all testbed data in both raw and engineering units. The computer communicates (i.e., send commands entered in the GUI and receive data) with the main testbed controller via Ethernet. It also communicates with the SMIRF control system. Finally, the computer will maintain a database of TA unique identification numbers along with corresponding pressure and temperature cycle data.

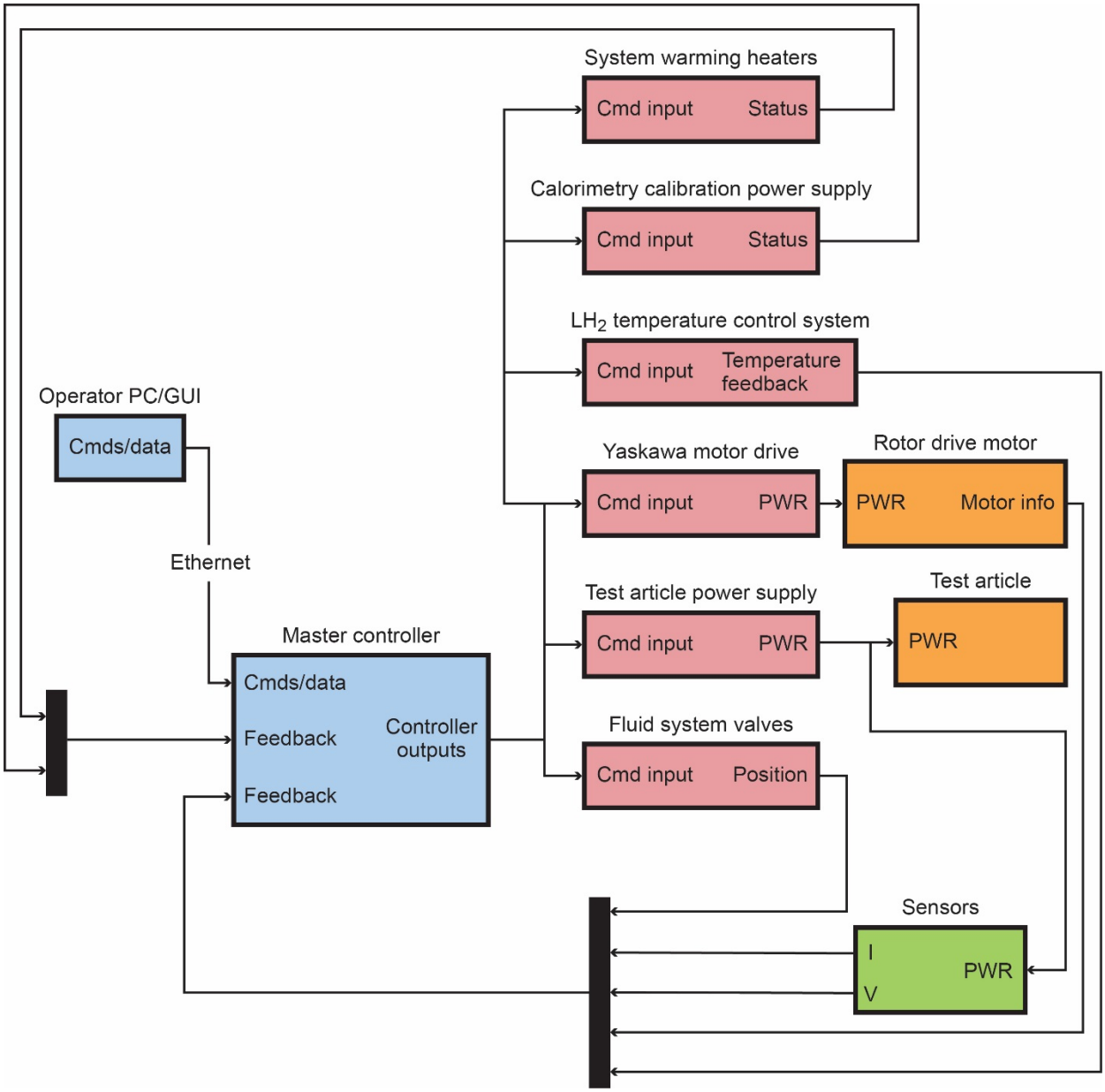

Figure 27.—Control system architecture, where Cmd is command, GUI is graphical user interface, I is current, PC is personal computer, PWR is power, and V is voltage.

The GUI is the testbed operator interface. From here, the operator establishes operating set points, certain limits, and test parameters. The GUI includes a combination mode selector and indicator, a means of entering set points, a means of issuing testbed commands, the display of test data, conspicuous display of operator alerts, which are pertinent to the prevailing mode of operation, and display component status in the DAQ computer screens.

The main testbed controller operates the testbed. It receives commands from the computer, which it processes to directly control components such as flow control valves, sends set points to stand-alone controllers, such as the rotor drive motor speed controller, and issues discrete commands and signals to turn components on or off, such as solenoid valves. Additionally, it receives all testbed-conditioned sensor data as well as data from stand-alone controllers, processes that data (e.g., perform calculations, convert to engineering units), and acts on the results according to preestablished algorithms. All of this information is accessible to the computer for subsequent display on the GUI. Furthermore, during test operations, the testbed controller ensures enforcement of permissives and interlocks, and continuously monitors for conditions that require either an alarm or shutdown.

There are seven modes of operation for the control system, including safe mode, magnetic field mapping mode, checkout mode, operations validation mode, calorimetry calibration heater mode, TA type A test mode, and TA type B test mode. Conditions for each of these seven modes are outlined in Appendix E.

10.0 Conclusions

A new LH_2-based testbed has been designed to measure alternating current (AC) losses of superconductors between the range of 18 to 28 K using LH_2 but easily extensible to 95 K using GHe or LN_2 as a working coolant. This document outlines the test capabilities, test parameter ranges, and details of each of the testbed subsystems, including test articles (TAs), core rig, power, fluids, instrumentation and data acquisition (DAQ), and control subsystems. While the target application is 20 K MgB_2 stator coils, the rig can accommodate low and high critical temperature (T_C) superconductors. The rig can handle both AC as well as direct current (DC) testing, perform AC loss testing with no-injection (induced current only) as well as injection current testing, and can accommodate a plethora of different sized and shaped wire, tape, cable, and coil TAs. The system is designed for the following test parameters: injected current (0 to 400 A), frequency (0 to 400 Hz), magnetic field (0 to 0.6 T), phase angle between induced voltage and injected current (–180° to 180°), and AC power loss (5 to 30 W). The new spin rig builds upon the existing spin rig capabilities in several ways as outlined previously.

Appendix A.—Nomenclature

1D	one-dimensional
3D	three-dimensional
A	alarms
AC	alternating current
ASME	American Society of Mechanical Engineers
B&PV	Boiler and Pressure Vessel
BLI	boundary layer ingestion
BSCCO	bismuth strontium calcium copper oxide
CCPS	calorimetry calibration power supply
CFD	computational fluid dynamics
Cmd	command
CSA	Canadian Standards Association
DAQ	data acquisition
DC	direct current
EOS	equation of state
FS	full scale
GUI	graphical user interface
I	current
ICE	Integrated Cryogenically Cooled Experiment
I.D.	inner diameter
LCF	low-cycle fatigue
LH_2	liquid hydrogen
LHe	liquid helium
LN_2	liquid nitrogen
NEC	National Electric Code
NFPA	National Fire Protection Agency
O.D.	outer diameter
OFHC	oxygen-free high thermal conductivity copper
P&ID	process and instrumentation diagram
PWM	pulse width modulation
PWR	power
RRR	residual resistance ratio
S	shutdowns
SAM	spin-around-magnet
SMiRF	Small Multipurpose Research Facility
SRSS	square root sum of squares
TA	test article
TAPS	test article power supply
V	voltage
VCR	variable compression ratio
VFD	variable frequency drive
VJ	vacuum jacketed
YBCO	yttrium barium copper oxide

Symbols

A	area, m²
A_B	acceleration, m/s²
B	peak magnetic field
C_p	specific heat, J/Kg•K
d	diameter, μm
d_{eff}	effective diameter
F	peak stress
f	frequency, Hz
h	enthalpy, J/kg
I_C	critical current
I_{ITA}	test article injected current
I_{load}	load current
I_T	injected transport current
I_{TA}	test article current
J	current density, A/m²
l	fraction of wire cross section made of superconducting filament
L	inductance
$\dot{m}$	mass flow rate, kg/s
n	sequence number
P	pressure, Pa
P_b	primary bending stress
P_{CE}	coolant exit pressure
P_{CS}	coolant supply pressure
P_L	primary local stress
P_m	primary membrane stress
P_{out}	output pressure
Q	secondary stress
$\dot{Q}$	heat rate, W
q_R	rotor position
q_r	motor rotation, rpm
Q_{TA}	predicted test article losses
S_m	ASME code material stress limit
S_u	ultimate stress
T	temperature, K
T_C	critical temperature
T_{CE}	coolant exit temperature
T_{CS}	coolant supply temperature (LH_2)
T_{out}	output temperature
t	time
t_p	twist pitch of superconducting filament, mm
U	uncertainty
V	volume, m³
$\dot{V}$	volumetric flow rate, m³/s
V_{cmd}	command voltage
V_{load}	load voltage
V_{TA}	test article voltage

V_{TAPS}	test article power source voltage
V_w	entire wire volume for motor or generator
W	power, W
WF_{ITA}	test article injected current waveform
μ_0	permeability of free space, m•kg/s²A²
ρ	density
ρ_n	transverse matrix resistivity, Ω•cm
φ	test article injected current phase angle
ϕ	alternating current phase angle, dimensionless
ω	speed
ω_r	rotor speed

Subscripts

AC	alternating current
C	critical
eoupling	coupling losses
e	injected current
eddy current	eddy current losses
f	superconducting filament through wire
hysteresis	hysteresis losses
n	sequence number
other	other losses
sx	surface
T	transport
total	total losses
transport	current transport losses
vv	vacuum
w	wire

Appendix B.—Thermal Analysis

To optimize thermal design, a detailed thermal model was developed using ANSYS® (ANSYS, Inc.) and a one-dimensional (1D) computational fluid dynamics (CFD) model using the three-dimensional (3D) model shown in Figure B.1. Details of the thermal boundary conditions and assumptions used in the model are shown in Figure B.2. Results of the thermal model are shown in Table B.1. As shown, approximately 2 W of parasitic heat leak into a test article (TA) was calculated with the thermal model, which was deemed an acceptable amount based on calculated alternating current (AC) losses.

To size the individual heaters, two cases were run as shown in Table B.2, at an ambient 274 and 293 K. The colder ambient was the driving case. Although not shown, the back iron heater was supplied with an 8-kW heater to reduce posttest warmup times to less than an hour.

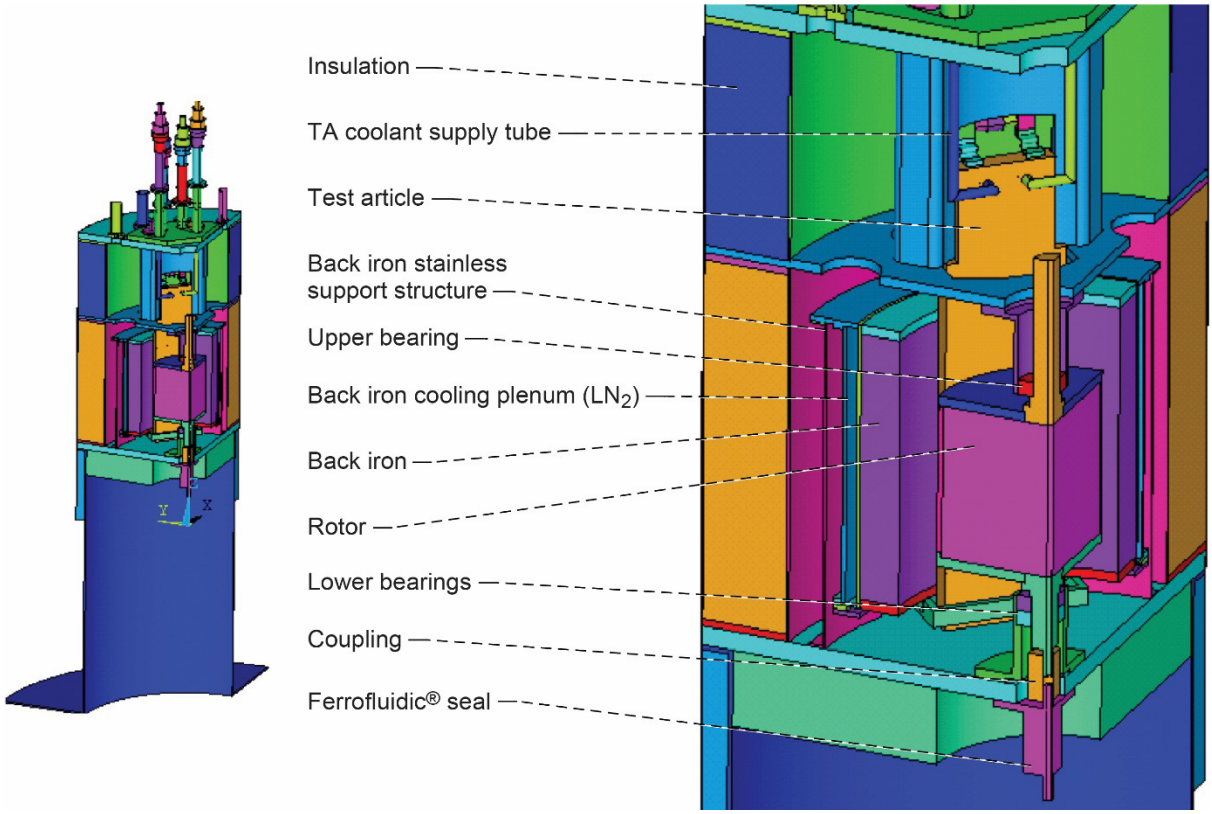

Figure B.1.—Thermal model, where TA is test article.

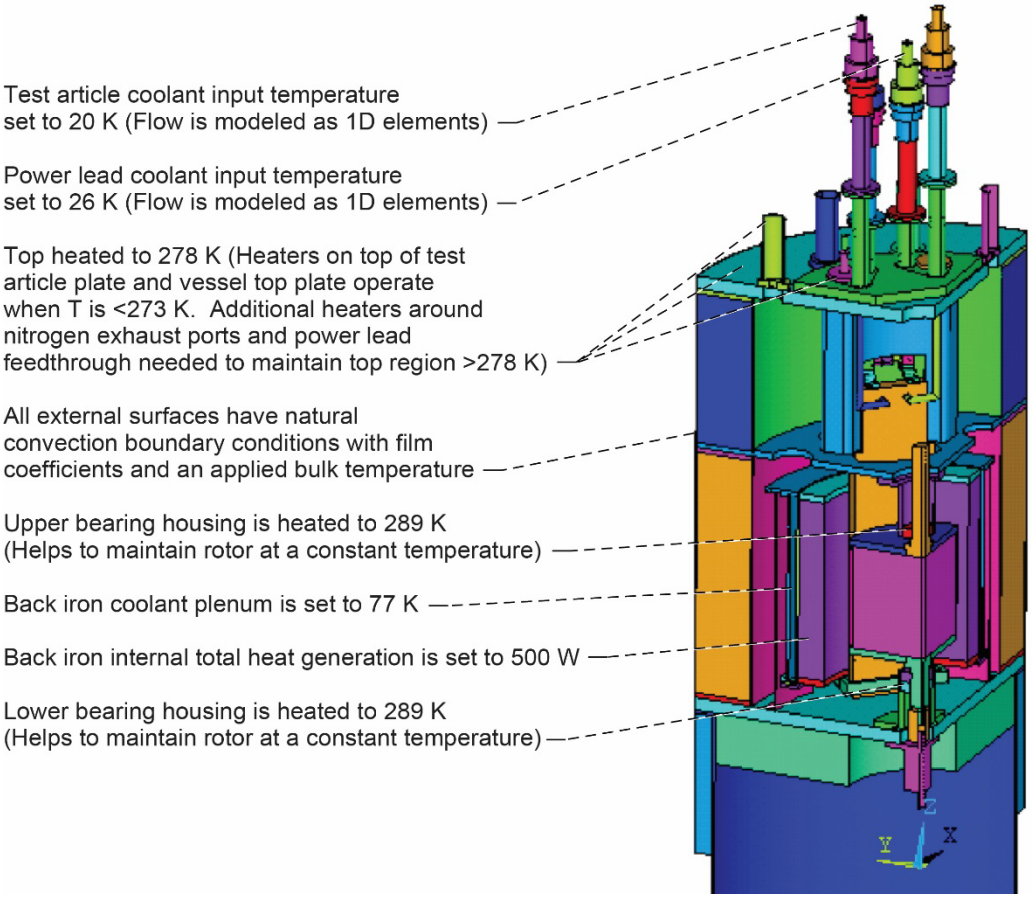

Figure B.2.—Thermal model boundary conditions, where TA is test article.

TABLE B.1.—COMPUTED PARASITIC HEAT LEAK

Source	Heat leak, W
Radiation, vessel bottom volume	0.381
Radiation, vessel top volume	0.080
Conduction, vessel bottom volume	0.462
Conduction, vessel top volume	1.064
Total	1.987

TABLE B.2.—REQUIRED HEATER POWER

Component and/or location	Power at 293 K ambient, W	Power at 274 K ambient, W
Upper bearing support	3.1	7.7
Lower bearing support	8.9	32.4
Vessel top plate	0	33.9
One GN_2 vent	663.5	680.1
One test article power lead	566.3	589.5
Total	1,242	1,343

Appendix C.—Structural Dynamic Analysis

A four-pronged approach was used to perform structural dynamic analysis of the core rig:

(1) A modal analysis of the test rig was performed by modeling the vessel, skirt, rotor, and bearings to determine the important modes based on mass participation.
(2) A whirl stability evaluation was performed at the minimum and maximum motor accelerations.
(3) A harmonic analysis was performed to evaluate the critical modes to determine the loading on the bearings at the critical speeds.
(4) A transient dynamic analysis was performed by accelerating the rotor through the entire speed range, plus 20 percent (0 to 7,200 rpm) to validate rotor displacements and bearing forces.

ANSYS® was used to perform rotor dynamics analysis. Figure C.1 shows the test rig and grid used for modal analysis. The three-dimensional (3D) surface model modes were evaluated using the surface and line models of the shell and rotor by meshing the vessel with SHELL93, the rotor with BEAM4s and MASS21 for the masses. For stability, harmonic, and transient analyses, BEAM4 elements were replaced with BEAM188. Simplifying assumptions made in the analysis are as follows:

- Bearings are modeled as linear springs—1.054 GPa (152,861 lbf/in) lower lateral and 10.04 GPa (1,457,230 lbf/in) vertical, upper lateral 1.25 GPa (181,925 lbf/in)
- Vessel housing and plate stiffness is appropriately modeled using shells
- Rotor imbalance is 0.0353 N for the harmonic and transient evaluations
- Rotor is modeled as a beam and the mass is applied as mass elements along the shaft

Results for modal analysis frequencies are shown in Table C.1 across the range of rotor speeds. Whirl stability analysis is presented in Table C.2. Harmonic analysis is shown in Table C.3 for the top and bottom bearings where square root sum of squares (SRSS) forces are also shown.

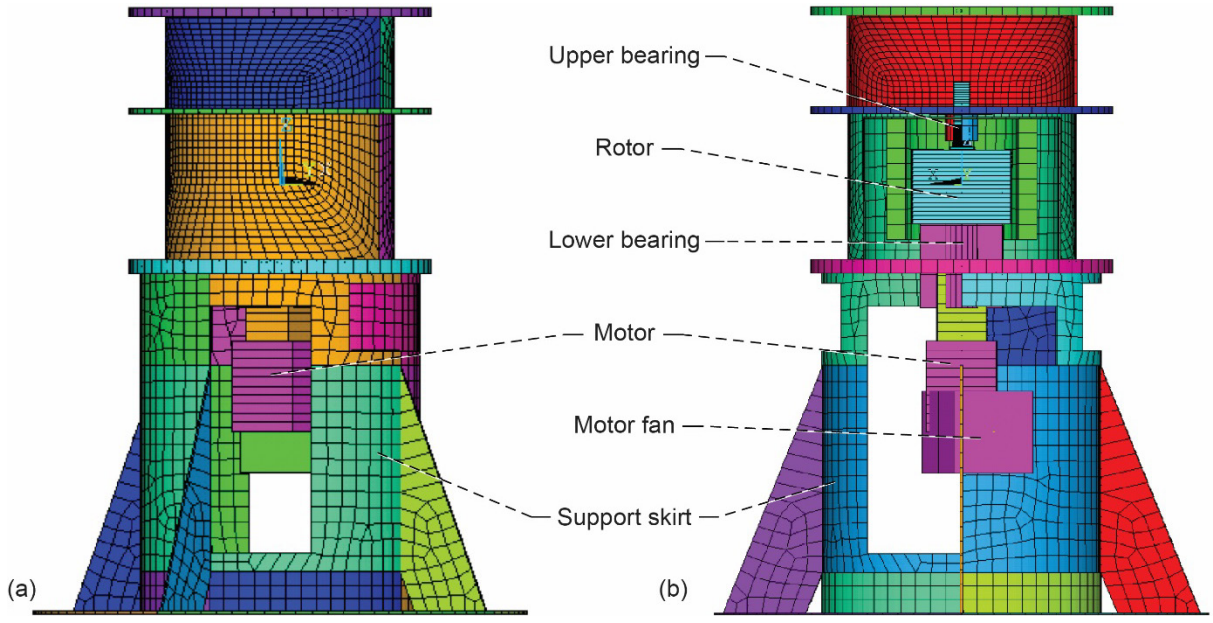

Figure C.1.—Test rig modal analysis model. (a) Full model. (b) Cutaway model.

TABLE C.1.—ROTOR (ROT) MODAL ANALYSIS

Effective mass sum, kg				2.4226	2.3672	2.4500	522.53	653.94	265.68
Mode	Frequency, Hz	Period, s	Frequency, rpm	Effective mass, kg					
				X	Y	Z	ROTX	ROTY	ROTZ
1	12.65	0.079	759.08	0.086272	2.172995	0.000045	0.000236	3.844605	0.053703
2	20.81	.048	1,248.7	2.201441	0.060525	.000026	2.112682	2.352064	.094552
3	25.12	.040	1,507.3	.011915	.095602	.024268	373.760000	8.508136	.045490
4	26.05	.038	1,562.8	.022067	.000499	.001217	9.909818	383.411818	2.858259
5	35.42	.028	2,125.4	.000132	.000645	2.353577	2.193273	0.338567	.076077
6	50.62	.020	3,037.2	.000047	.004919	.000009	30.085773	.016143	.000824
7	50.77	.020	3,046.4	.001843	.000090	.000001	.145515	36.326682	.001316
8	59.96	.017	3,597.3	.000000	.000000	.000022	.000654	.000292	.000007
9	68.95	.015	4,137.1	.000034	.000182	.000198	.441910	.018936	.001679
10	71.54	.014	4,292.5	.000028	.000800	.000028	.423226	.087757	.338279
11	71.87	.014	4,312.0	.001348	.000000	.000016	.056203	.378406	127.279091
12	72.00	.014	4,320.3	.001584	.000015	.000023	.006749	.196221	84.019545
13	84.70	.012	5,082.0	.001092	.009196	.000040	36.340455	30.699091	.001971
14	93.65	.011	5,618.8	.049836	.000444	.000155	.281696	103.941818	.001545
15	95.55	.010	5,733.2	.000091	.000000	.044618	.003579	.224386	5.682682
16	107.30	.009	6,438.2	.000317	.011547	.000008	36.559636	3.796364	.016433
17	118.86	.008	7,131.8	.000096	.000001	.025706	.011721	.200169	45.066045
18	124.93	.008	7,495.5	.000716	.000016	.000002	.105065	1.385382	.006668
19	125.00	.008	7,499.9	.000089	.000222	.000006	.670073	.077962	.010864
20	133.97	.007	8,038.4	.043588	.008607	.000022	28.997500	79.317273	.124546

TABLE C.2.—WHIRL STABILITY ANALYSIS

Whirl mode	1 time spin, rpm	2 times spin, rpm	3 times spin, rpm	4 times spin, rpm	5.5 rad/s², rpm	20 rad/s², rpm
-	None	None	None	None	None	None
1	None	None	None	None	None	None
2	None	None	None	None	None	None
3	3,480.3	1,642.2	1,083.6	806.5	3,450	850
4	None	None	2,768.2	2,059.2	None	2,100
5	None	None	None	None	None	None
6	None	None	None	None	None	None
7	None	None	None	None	None	None
8	None	None	None	None	None	None
9	None	None	None	None	None	None

TABLE C.3.—HARMONIC ANALYSIS

Top bearing					Bottom bearing				
ω, rpm	*F*x[a], kg	*F*y, kg	*F*z, kg	SRSS[b] (*F*x, *F*y), kg	ω[c], rpm	*F*x, kg	*F*y, kg	*F*z, kg	SRSS (*F*x, *F*y), kg
759.1	–2.6	–2.6	6.4	3.7	759.1	–2.4	–2.4	134.6	3.4
1,248.7	–7.1	–6.9	6.4	10.0	1,248.7	–6.4	–6.6	134.6	9.2
1,248.7	–10.4	–10.1	6.4	14.5	1,248.7	–9.3	–9.7	134.6	13.4
1,562.8	–11.2	–10.8	6.4	15.6	1,562.8	–10.0	–10.4	134.6	14.4
2,125.4	–20.9	–19.9	6.4	28.9	2,125.4	–18.3	–19.2	134.7	26.6
3,037.2	–43.2	–40.3	6.4	59.1	3,037.2	–36.8	–39.3	134.7	53.8
3,046.4	–43.5	–40.5	6.4	59.4	3,046.4	–37.0	–39.5	134.7	54.1
4,312.0	–88.5	–80.1	6.5	119.4	4,312.0	–72.2	–78.6	134.8	106.7
4,320.3	–88.8	–80.4	6.5	119.8	4,320.3	–72.5	–78.9	134.8	107.1
5,082.0	–124.0	–110.4	6.5	166.0	5,082.0	–98.6	–108.4	134.9	146.5
5,618.8	–152.5	–134.2	6.5	203.1	5,618.8	–119.0	–131.7	135.0	177.5
6,000.0	–174.6	–152.3	6.5	231.7	6,000.0	–134.6	–149.3	135.1	201.0
6,438.0	–201.9	–174.5	6.5	266.9	6,438.0	–153.4	–170.7	135.1	229.5
7,131.6	–249.6	–212.5	6.5	327.8	7,131.6	–185.2	–206.9	135.2	277.7
7,200.0	–254.6	–216.5	6.5	334.2	7,200.0	–188.5	–210.6	135.3	282.6

[a]Peak stress of x.
[b]Square root sum of squares.
[c]Speed.

A summary of results is as follows: the modal analysis predicts a mass participation of 48 percent of the total mass around 4,300 rpm, which is considered a region of speed to avoid. The Campbell Diagram analysis predicts stability for the whirl modes, despite critical speeds for

- Whirl mode 3 at 3,450 rpm with an acceleration of 5.5 rad/s^2 (motor nominal acceleration)
- Whirl mode 3 at 850 rpm with an acceleration of 20.0 rad/s^2 (motor maximum acceleration)
- Whirl mode 4 at 2,100 rpm with an acceleration of 20.0 rad/s^2

The transient analysis predicts a perturbation at 4,200 rpm, similar to the modal analysis, and perhaps a detrimental response beyond the 120-percent load range at 7,200 rpm. The transient analysis also shows that 5.5 rad/s² is adequate to safely pass through the critical speed at 4,200 rpm, however, the rotor becomes unstable above 7,200 rpm. Therefore, the rotor will not dwell around 4,200 or 4,300 rpm (~70 Hz) and will not be operated outside the 120-percent range (7,200 rpm) of rotational velocity.

Appendix D.—Structural Analysis

A four-pronged approach was used to perform structural analysis on the core rig

- The three-dimensional (3D) model was imported into ANSYS® and meshed with quadratic elements (SOLID95).
- Temperatures, dynamic loads, internal and external pressure, and dead weight of components were applied to the system in various load combinations to correlate with the loading conditions from American Society of Mechanical Engineers Boiler and Pressure Vessel (ASME B&PV) code Section VIII, Division II.
- The primary and secondary stresses were evaluated based on linearized stresses via cut lines in ANSYS®.
- ASME B&PV Section III, Division 1, Subsection NG design factors were included in the structural analysis and form the basis for the planned weld inspection.

Figure D.1 and Figure D.2 show the load cases with descriptions. Table D.1 shows the buckling and plenum working pressure calculations. Table D.2 and Table D.3 show the summary of results for the structural analysis and welds, respectively. As shown, the primary and secondary stress results for the vessel and welds are low, with significant margin. The fatigue stresses are also low and below the endurance limit for 304 stainless steel. The axial compression stresses are low for all components in compression, therefore, buckling is not an issue. The maximum working pressure for the back iron plenum is over 2.07 MPa (300 psia), while the nominal operating pressure is 101.4 kPa (14.7 psia).

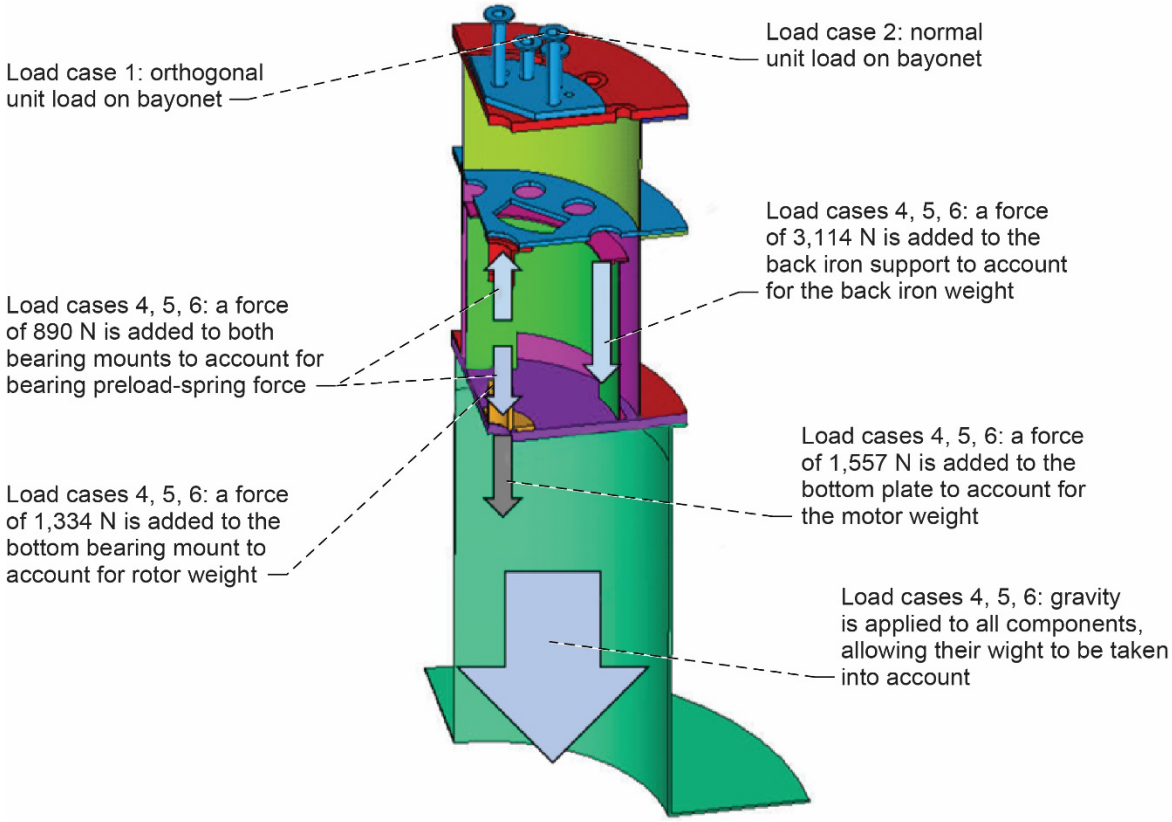

Figure D.1.—Analyzed load cases I.

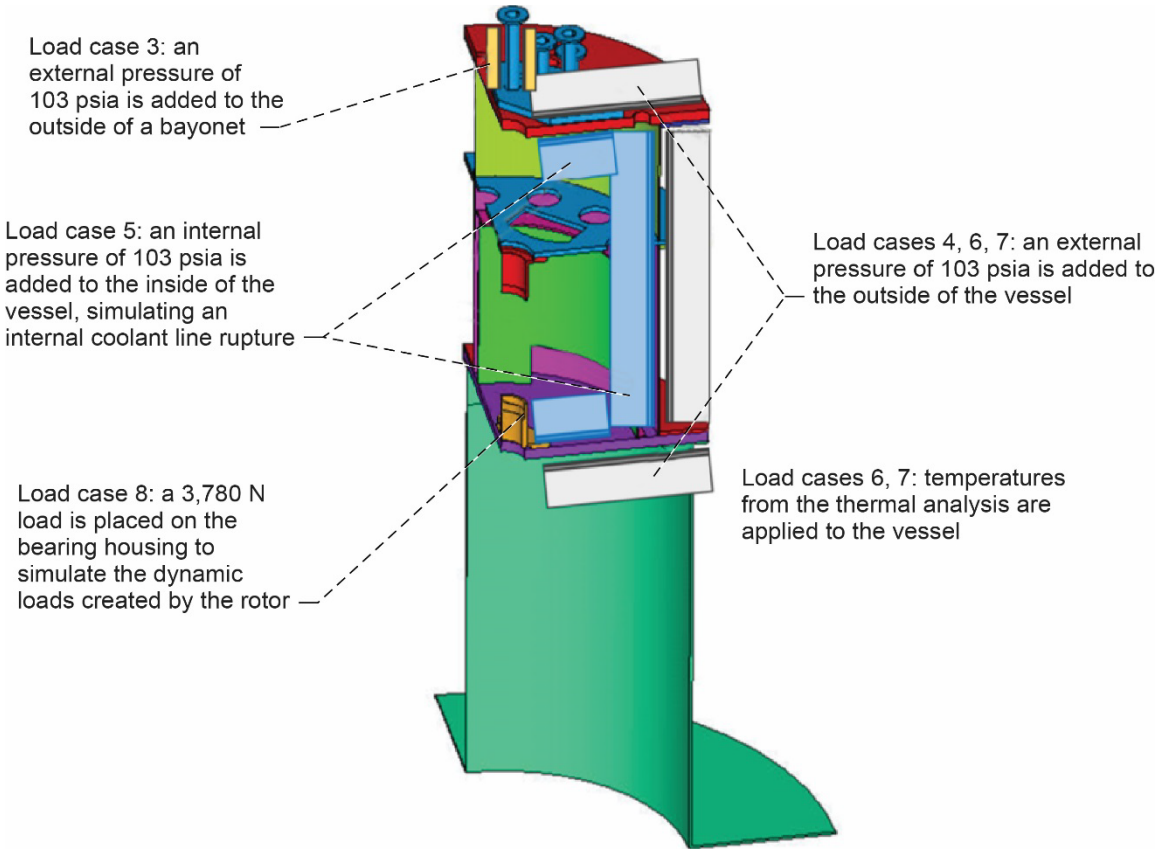

Figure D.2.—Analyzed load cases II.

TABLE D.1.—BUCKLING AND PLENUM WORKING PRESSURE CALCULATIONS

	Hoop stress (pressure), MPa	Max. working pressure, psi	Total compressive force, kN	Max. allowable buckling force, MN	Max. allowable buckling stress, GPa	A factor	Compressive stress (total), MPa	B factor (max. longitudinal stress) from, MPa	Compression factor
Top cylinder	11.420	NA	83	8.27×10^{2}	118	0.001122	17.540	62.052813	3.5
Bottom cylinder	11.420	NA	84	2.23×10^{3}	318	.001122	17.670	62.052813	3.5
Skirt	NA	NA	5	6.66×10^{2}	39	.001838	0.268	75.842327	283.3
Back iron support	NA	NA	3	7.12×10^{2}	118	.001302	.515	68.94757	133.9
Back iron plenum	6.070	2.4	–4	8.14×10^{2}	98	NA	NA	NA	NA

TABLE D.2.—STRUCTURAL ANALYSIS VESSEL SUMMARY

Summary of results for the vessel					
Loading condition[a,b]	Stress category	Stress[c]/usage	Allowable stress[c,d]/usage		Margin[e]
Normal	P_m[f]	13.79	S_m[g]	137.9	9.12
	P_L[h] + P_b[i]	15.86	$1.5S_m$	206.8	12.16
	$P_L + P_b + Q$[j]	40.68	$3.0S_m$	413.7	9.16
	$P_L + P_b + Q + F$[k] (LCF[l])	44.46	<1.0	6.9	NA
	High cycle fatigue	11.03	<endurance limit	93.8	7.72
Abnormal	P_m	13.79	Lesser of $2.4S_m$ or $0.7S_u$[m]	330.9	23.28
	$P_L + P_b$	14.48	Lesser of $3.6S_m$ or $1.05S_u$	496.4	33.56

[a]Normal condition is for operation with internal vacuum while the TA is in a steady-state cold condition.
[b]Abnormal condition may occur if there is a leak of coolant into the vessel generating internal pressure of 96.5 kPa (14 psi).
[c]Stresses are in units of MPa.
[d]Based on SA-240 Section II, Part D, type 304 stainless steel at 294 K.
[e]Margin of safety = (allowable/value) – 1.0.
[f]Primary membrane stress.
[g]ASME code material stress limit.
[h]Primary local stress.
[i]Secondary stress.
[j]Secondary stress.
[k]Peak stress.
[l]Low cycle fatigue.
[m]Ultimate stress.

TABLE D.3.—STRUCTURAL ANALYSIS VESSEL WELD SUMMARY

Summary of results for the welds					
Loading condition[a,b]	Stress category	Stress[c]/usage	Allowable stress[c,d]/usage		Margin[e]
Normal	P_m[f]	15.17	S_m[g]	55.2	2.71
	P_L[h] + P_b[i]	39.30	$1.5S_m$	82.7	1.10
	$P_L + P_b + Q$[j]	72.39	$3.0S_m$	165.5	1.29
	$P_L + P_b + Q + F$[k] (LCF[l])	78.29[m,n]	<1.0	6.9	NA
	High cycle fatigue	25.51	<endurance limit	93.8	2.65
Abnormal	P_m	19.31	Lesser of $2.4S_m$ or $0.7S_u$[o]	132.4	5.97
	$P_L + P_b$	47.57	Lesser of $3.6S_m$ or $1.05S_u$	198.6	3.16

[a]Normal condition is for operation with internal vacuum while the TA is in a steady-state cold condition.
[b]Abnormal condition may occur if there is a leak of coolant into the vessel generating internal pressure of 96.5 kPa (14 psi).
[c]Stresses are in units of MPa.
[d]Based on SA-240 Section II, Part D, type 304 stainless steel at 294 K.
[e]Margin of safety = (allowable/value) – 1.0.
[f]Primary membrane stress.
[g]ASME code material stress limit.
[h]Primary local stress.
[i]Primary bending stress.
[j]Secondary stress.
[k]Peak stress.
[l]Low cycle fatigue.
[m]Stress range is below the endurance limit of 9.38 MPa (13.6 ksi).
[n]Applied a weld fatigue factor (f) of 4.0 per table NG-3352-1.
[o]Ultimate stress.

Appendix E.—Control Modes of Operation

E.1 Safe Mode

Table E.1 outlines conditions for safe mode, the default mode of operation at power up and shutdown. In this mode, all set points are zeroed. The controller self-checks at power on. The operator is alerted to any temperature within the core rig that is below freezing. Safe mode is entered at any time from any other mode via operator-issued command or autonomous controller action when an established threshold limit is reached.

E.2 Magnetic Field Mapping Mode

Table E.2 outlines conditions for magnetic field mapping mode. Figure E.1 shows the system-level diagram for this mode. The purpose of this mode is to obtain a high-resolution magnetic field strength map of the entire vacuum gap and the annular volume bounded on the inside by the rotor outer diameter (O.D.), on the outside by the iron core inner diameter (I.D.), and on the ends by physical stops. Whenever a magnetic field mapping is performed, the controller is switched to this mode. While in this mode, the control system ensures the conditions outlined in Table E.2. The operator is alerted if the bearing housing accelerations or temperatures approach the limit and the system enters safe mode.

TABLE E.1.—SAFE MODE

System	Status
LH_2	Fail-safe, inhibited
LN_2	Fail-safe, inhibited
Vacuum	Fail-safe, inhibited
Purge (GHe, GN_2)	Operational
Vent	Operational
LH_2 temperature control system	Inhibited
Test article power supply	Inhibited
Calorimetry calibration power supply	Inhibited
Rotor drive system	Inhibited
Instrumentation and data acquisition	Operational
Heaters	Operational

TABLE E.2.—MAGNETIC FIELD MAPPING MODE

System	Status
LH_2	Fail-safe, inhibited
LN_2	Fail-safe, inhibited
Vacuum	Fail-safe, inhibited
Purge	Fail-safe, inhibited
Vent	Fail-safe, inhibited
LH_2 temperature control system	Inhibited
Test article power supply	Inhibited
Calorimetry calibration power supply	Inhibited
Rotor drive system	Operational
Instrumentation and data acquisition	Operational
Heaters	Operational

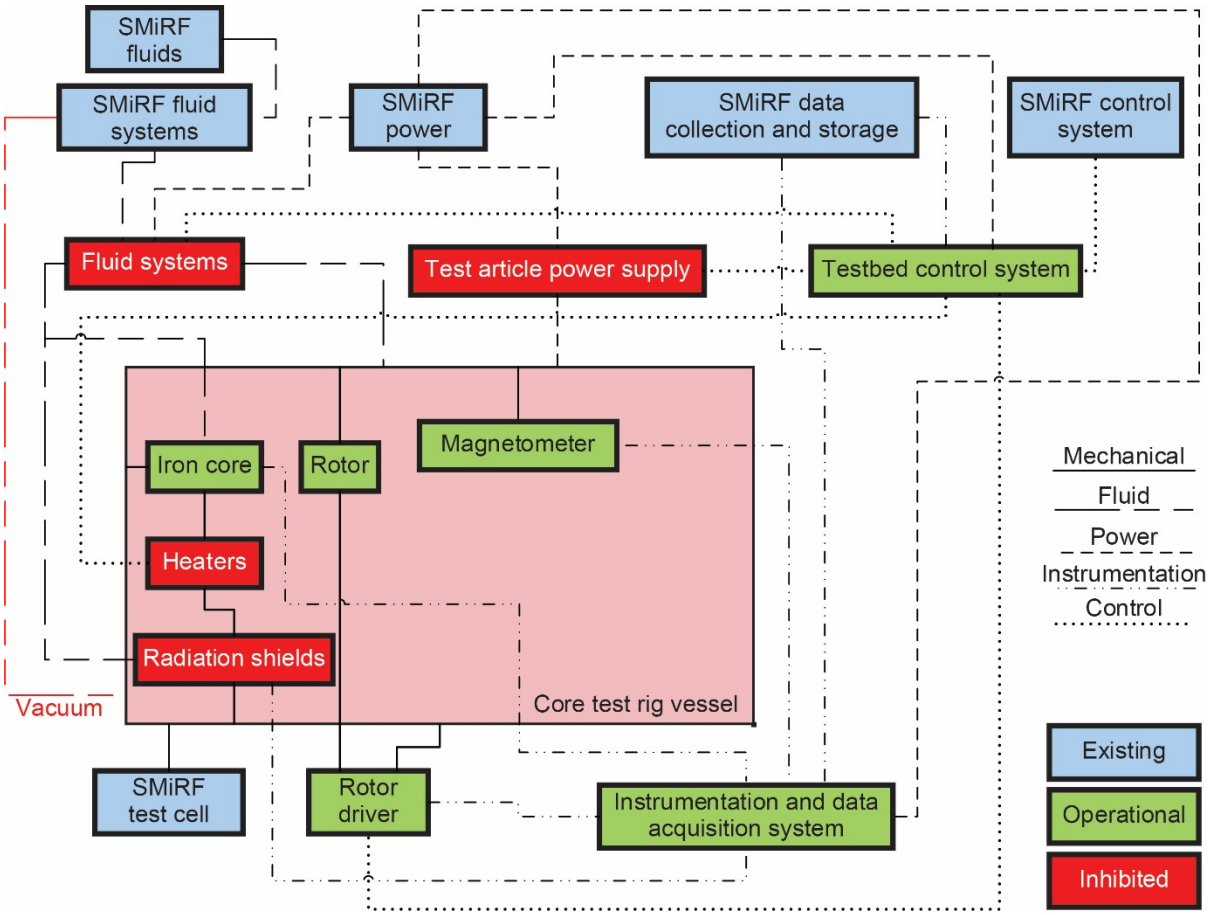

Figure E.1.—Magnetic field mapping mode system diagram, where SMiRF is Small Multipurpose Research Facility.

TABLE E.3.—CHECKOUT MODE

System	Status
LH_2	Inhibited
LN_2	Operational
Vacuum	Operational
Purge	Operational
Vent	Operational
LH_2 temperature control system	Inhibited
Test article power supply	Inhibited
Calorimetry calibration power supply	Inhibited
Rotor drive system	Inhibited
Instrumentation and data acquisition	Operational
Heaters	Operational

E.3 Checkout Mode

Table E.3 outlines conditions for checkout mode. Figure E.2 shows the system-level diagram for this mode. Checkout serves as a means to ensure that procedures and instructions are correct, functions and features are present, and performance is as intended and necessary for both nominal and off-nominal situations prior to conducting test article (TA) operations. Example checkout tests include pump down

tests that ensure that the rig is leak free at the operating pressure of 10^{-5} torr, and cold shocks, which ensure that joints that will be wetted with cryogens during normal operation are sound and remain leak free during operations. In this mode, the operator is alerted if chill or warm rates, TA inlet pressure, or LH_2 temperature control system dewar pressure approaches the predefined limit and the system enters safe mode.

E.4 Operations Validation Mode

Table E.4 outlines conditions for operations validation mode. Figure E.3 shows the system-level diagram for this mode. This mode is used to validate nominal and off-nominal operations:

- Ensure that all alarms, shutdowns, permissives, interlocks, and operational hazard controls are present and functioning as intended
- Evaluate, refine, or fix related written operations procedures and/or instructions
- Operator training
- Ensure that the relevant aspects of the testbed operator interface are complete and correct
- Acquire baseline testbed operational data for entire operating envelope

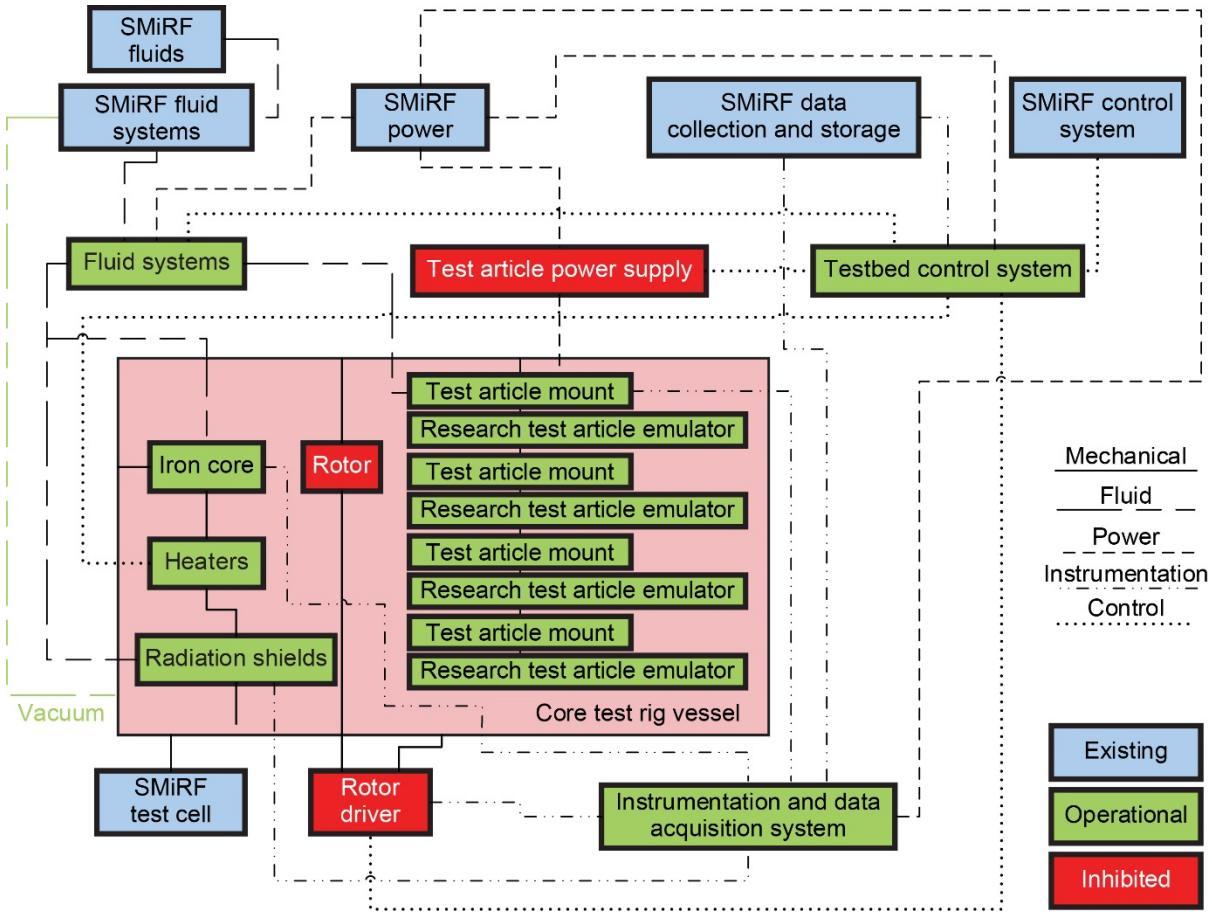

Figure E.2.—Checkout mode system diagram, where SMiRF is Small Multipurpose Research Facility.

In this mode, the operator is alerted if set points are violated or limits are approached for the following:

(1) Key core test rig surface temperatures
(2) Chill and warm rates
(3) TA inlet pressure (indication of possible two-phase flow)
(4) TA LH_2 exit conditions
(5) TA supply temperature
(6) LH_2 temperature control system dewar pressure
(7) Rotor speed
(8) Test article injection current
(9) Bearing housing acceleration
(10) Bearing housing temperature, either too cold or too warm

If any of these approach the predefined limit, the system enters safe mode.

E.5 Calorimetry Calibration Mode

Table E.5 outlines conditions for calorimetry calibration mode. Figure E.4 shows the system-level diagram for this mode. Whenever it is necessary to verify or calibrate calorimetry measurements, the controller is switched to this mode. Calorimetry calibration mode is used to validate nominal and off-nominal operations. The operator is alerted if set points are violated or limits are approached for the same 10 measurements in Section E.4. If any of those approach the predefined limit, the system enters safe mode.

E.6 Type A Test Article (TA) (Straight Wire Samples) Test Mode

Table E.6 outlines conditions for straight wire sample mode. Recall that the difference between type A and type B TAs is purely geometrical. This mode is also used to validate nominal and off-nominal operations. The operator is alerted if set points are violated or limits are approached for the same 10 measurements in Section E.4. If any of those approach the predefined limit, the system enters safe mode.

TABLE E.4.—OPERATIONS VALIDATION MODE

System	Status
LH_2	Operational
LN_2	Operational
Vacuum	Operational
Purge	Operational
Vent	Operational
LH_2 temperature control system	Operational
Test article power supply	Operational
Calorimetry calibration power supply	Inhibited
Rotor drive system	Operational
Instrumentation and data acquisition	Operational
Heaters	Operational

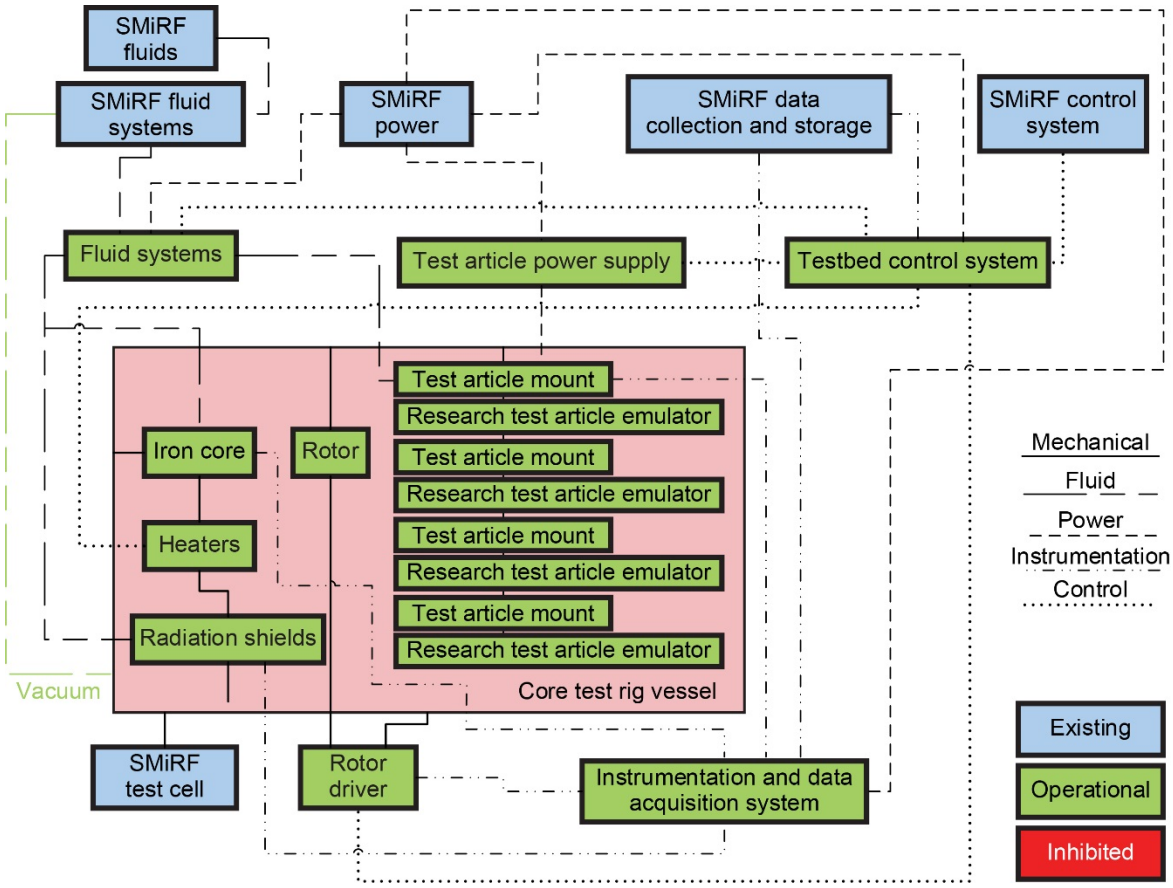

Figure E.3.—Operations validation mode system diagram, where SMiRF is Small Multipurpose Research Facility.

TABLE E.5.—CALORIMETRY CALIBRATION MODE

System	Status
LH_2	Operational
LN_2	Operational
Vacuum	Operational
Purge	Operational
Vent	Operational
LH_2 temperature control system	Operational
Test article power supply	Inhibited
Calorimetry calibration power supply	Operational
Rotor drive system	Operational
Instrumentation and data acquisition	Operational
Heaters	Operational

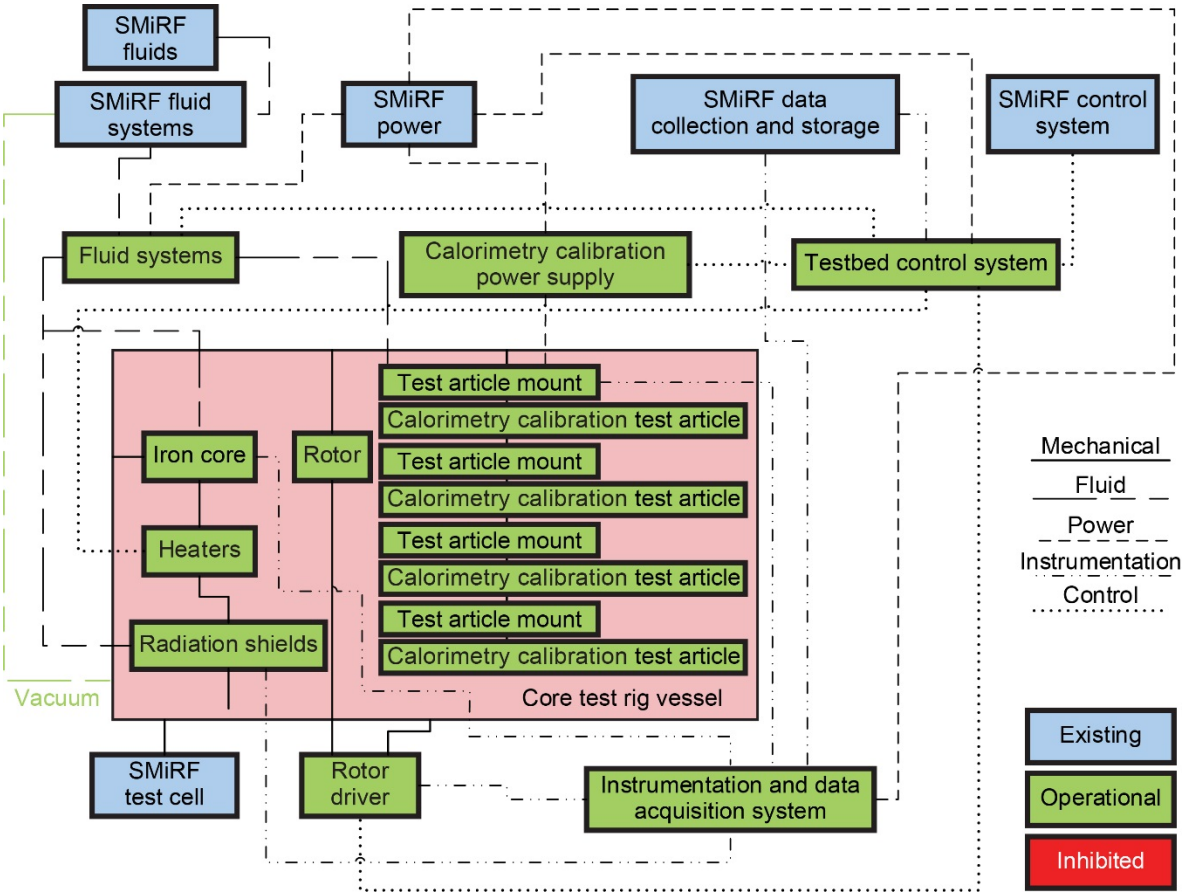

Figure E.4.—Calorimetry calibration mode system diagram, where SMiRF is Small Multipurpose Research Facility.

TABLE E.6.—STRAIGHT WIRE SAMPLE TEST MODE

System	Status
LH_2	Operational
LN_2	Operational
Vacuum	Operational
Purge	Operational
Vent	Operational
LH_2 temperature control system	Operational
Test article power supply	Inhibited
Calorimetry calibration power supply	Inhibited
Rotor drive system	Operational
Instrumentation and data acquisition	Operational
Heaters	Operational

Table E.7 and Table E.8 outline the methodology for obtaining data for static magnetic field tests (nonrotating rotor) and for time-varying magnetic field tests, respectively. Note that knowledge of the rotor angular position is required for 0-rpm tests. This is due to the nonuniform arrangement of the magnetic poles as shown in Figure 14.

E.7 Type B Test Article (TA) (Coil Samples) Test Mode

Table E.9 outlines conditions for coil sample test mode. This mode is also used to validate nominal and off-nominal operations. The operator is alerted if set points are violated or limits are approached for the same 10 measurements in Section E.4. If any of those approach the predefined limit, the system enters safe mode. Table E.10 and Table E.11 outline the methodology for obtaining data for static magnetic field tests (nonrotating rotor) and for time-varying magnetic field tests, respectively.

TABLE E.7.—TEST MATRIX FOR STATIC FIELD TESTS FOR TYPE A TEST ARTICLES (TAs)

Test point	LH_2 supply temperature, T_{CS}, 18 to 28 K	Rotor position, q_R, from field min. to field max.	Desired LH_2 ΔT, $T_{CS} - T_{CE}$[a], K	Predicted TA losses, Q_{TA}, W	Predicted LH_2 flow rate, $\dot{m}$, L/s
1	T_{CS}	Field min.	$(T_{CS} - T_{CE})$	Q_{TA1}	$\dot{m}_1$
↓		↓		↓	↓
n		Field max.		Q_{TAn}	$\dot{m}_n$

[a]Coolant exit temperature.

TABLE E.8.—TEST MATRIX FOR TIME-VARYING FIELD TESTS FOR TYPE A TEST ARTICLES (TAs)

Test point	LH_2 supply temperature, T_{CS}, 18 to 28 K	Rotor speed, ω_r, 100 to 6,000 rpm	Desired LH_2 ΔT, $T_{CS} - T_{CE}$[a], K	Predicted TA losses, Q_{TA}, W	Predicted LH_2 flow rate, $\dot{m}$, L/s
1	T_{CS1}	ω_{r1}	$(T_{CS} - T_{CE})_1$	Q_{TA1}	$\dot{m}_1$
↓		↓	↓	↓	↓
		ω_{rn}	$(T_{CS} - T_{CE})_n$	Q_{TAn}	$\dot{m}_n$
	↓	↓	↓	↓	↓
	T_{CSn}	ω_{r1}	$(T_{CS} - T_{CE})_1$	Q_{TA1}	$\dot{m}_1$
↓		↓	↓	↓	↓
n		ω_{rn}	$(T_{CS} - T_{CE})_n$	Q_{TAn}	$\dot{m}_n$

[a]Coolant exit temperature.

TABLE E.9.—STRAIGHT WIRE SAMPLE TEST MODE

System	Status
LH_2	Operational
LN_2	Operational
Vacuum	Operational
Purge	Operational
Vent	Operational
LH_2 temperature control system	Operational
Test article power supply	Operational
Calorimetry calibration power supply	Inhibited
Rotor drive system	Operational
Instrumentation and data acquisition	Operational
Heaters	Operational

TABLE E.10.—TEST MATRIX FOR STATIC FIELD TESTS FOR TYPE B TEST ARTICLES (TAs)

Test point	LH_2 supply temperature, T_{CS}, 18 to 28 K	Rotor position, q_r, from field min. to field max.	TA DC[a] injected current, I_{ITA}, 0 to 400 A	Desired LH_2 ΔT, $T_{CS} - T_{CE}$[b], K	Predicted test article losses, Q_{TA}, W	Predicted LH_2 flow rate, $\dot{m}$, L/s
1	T_{CS1}	Field min.	I_{ITA1}	$(T_{CS} - T_{CE})_1$	Q_{TA1}	$\dot{m}_1$
↓	↓	↓	↓	↓	↓	↓
			I_{ITAn}	$(T_{CS} - T_{CE})_n$	Q_{TAn}	$\dot{m}_n$
		↓	↓	↓	↓	↓
		Field max.	I_{ITA1}	$(T_{CS} - T_{CE})_1$	Q_{TA1}	$\dot{m}_1$
			↓	↓	↓	↓
			I_{ITAn}	$(T_{CS} - T_{CE})_n$	Q_{TAn}	$\dot{m}_n$
	↓	↓	↓	↓	↓	↓
	T_{CSn}	Field min.	I_{ITA1}	$(T_{CS} - T_{CE})_1$	Q_{TA1}	$\dot{m}_1$
			↓	↓	↓	↓
			I_{ITAn}	$(T_{CS} - T_{CE})_n$	Q_{TAn}	$\dot{m}_n$
		↓	↓	↓	↓	↓
		Field max.	I_{ITA1}	$(T_{CS} - T_{CE})_1$	Q_{TA1}	$\dot{m}_1$
			↓	↓	↓	↓
n			I_{ITAn}	$(T_{CS} - T_{CE})_n$	Q_{TAn}	$\dot{m}_n$

[a]Direct current.
[b]Coolant exit temperature.

TABLE E.11.—TEST MATRIX FOR TIME-VARYING FIELD TESTS FOR TYPE B TEST ARTICLES (TAs)

Test point	LH_2 supply temperature, T_{CS}, 18 to 28 K	Rotor speed, ω_r, 100 to 6,000 rpm	TA injected current, I_{ITA}, 1 to 400 A	TA injected current waveform, WF_{ITA}	TA injected current phase angle, φ, –180° to 180°	Desired LH_2 ΔT, $T_{CS} - T_{CE}$[a], K	Predicted TA losses, Q_{TA}, W	Predicted LH_2 flow rate, $\dot{m}$, L/s
1	T_{CS1}	ω_{r1}	I_{ITA1}	WF_{ITA1}	φ_1	$(T_{CS} - T_{CE})_1$	Q_{TA1}	$\dot{m}_1$
					↓		↓	↓
					φ_n		Q_{TAn}	$\dot{m}_n$
			↓	↓	↓	↓	↓	↓
			I_{ITAn}	WF_{ITAn}	φ_1	$(T_{CS} - T_{CE})_n$	Q_{TA1}	$\dot{m}_1$
					↓		↓	↓
					φ_n		Q_{TAn}	$\dot{m}_n$
		↓	↓	↓	↓	↓	↓	↓
		ω_{rn}	I_{ITA1}	WF_{ITA1}	φ_1	$(T_{CS} - T_{CE})_1$	Q_{TA1}	$\dot{m}_1$
					↓		↓	↓
					φ_n		Q_{TAn}	$\dot{m}_n$
			↓	↓	↓	↓	↓	↓
			I_{ITAn}	WF_{ITAn}	φ_1	$(T_{CS} - T_{CE})_n$	Q_{TA1}	$\dot{m}_1$
					↓		↓	↓
					φ_n		Q_{TAn}	$\dot{m}_n$
	↓	↓	↓	↓	↓	↓	↓	↓
	T_{CSn}	ω_{r1}	I_{ITA1}	WF_{ITA1}	φ_1	$(T_{CS} - T_{CE})_1$	Q_{TA1}	$\dot{m}_1$
					↓		↓	↓
					φ_n		Q_{TAn}	$\dot{m}_n$
			↓	↓	↓	↓	↓	↓
			I_{ITAn}	WF_{ITAn}	φ_1	$(T_{CS} - T_{CE})_n$	Q_{TA1}	$\dot{m}_1$
					↓		↓	↓
					φ_n		Q_{TAn}	$\dot{m}_n$
		↓	↓	↓	↓	↓	↓	↓
		ω_{rn}	I_{ITA1}	WF_{ITA1}	φ_1	$(T_{CS} - T_{CE})_1$	Q_{TA1}	$\dot{m}_1$
					↓		↓	↓
					φ_n		Q_{TAn}	$\dot{m}_n$
			↓	↓	↓	↓	↓	↓
			I_{ITAn}	WF_{ITAn}	φ_1	$(T_{CS} - T_{CE})_n$	Q_{TA1}	$\dot{m}_1$
					↓		↓	↓
n					φ_n		Q_{TAn}	$\dot{m}_n$

[a]Coolant exit temperature.

Appendix F.—Hazards, Interlocks, Permissives, Alarms, and Shutdowns

F.1 Hazards

For LH_2 service, three main risks have been identified:

(1) If a rupture disk bursts, there is still the presence of a flammable mixture in the core rig vessel. This situation is not plausible prior to the rupture disk burst, since normal operation is at a background pressure of 10^{-5} torr. The rig goes into shutdown at 10^{-4} torr; this pressure level corresponds to only 4.5 g of hydrogen.
(2) Presence of a flammable mixture external to the test rig.
(3) Large leaks within the core rig vessel that cause the rupture disk to burst and the vessel to vent into the test cell before rig shutdown would only occur for a brief period (seconds). For small leaks within the core rig vessel, the vacuum system is sized appropriately to continually pump down.

An additional third risk is low oxygen levels in the Small Multipurpose Research Facility (SMiRF) that could arise during any event, such as high concentrations of vented GN_2 during fill of the back iron plenum. This is a highly unlikely scenario since chilldown rates will be slow and controlled and due to open-door SMiRF test cell operation.

F.2 Interlocks

Three key interlocks exist:

(1) Cryogen cannot flow into the testbed unless the core rig vacuum levels are satisfied.
(2) The rotor cannot be driven unless sufficient coolant is flowing through the test article (TA).
(3) Current cannot be injected into the TA unless sufficient coolant is flowing through the TA.

F.3 Permissives

The only permissive is as follows: the TA pressure and temperature cycle data must be known before a test can be performed.

F.4 Alarms (A) and Shutdowns (S)

The following is a list of A and S:

(1) Bearing housing accelerations (A/S)
(2) Bearing temperature rise (A/S)
(3) Excessive chilldown or warmup rates (A/S)
(4) Excessive TA inlet pressure (A/S)
(5) High rotor speed (A/S)
(6) Excessively cold bearings (A/S)
(7) Fluctuating TA inlet temperature (A)
(8) Fluctuating TA inlet pressure (A)

If shutdown mode is entered, only the controller instrumentation, data acquisition (DAQ), heaters, purge, and vent remain operational.

References

1. Brown, Gerald V.: Weights and Efficiencies of Electric Components of a Turboelectric Aircraft Propulsion System. AIAA 2011–225, 2011.
2. Jansen, Ralph H., et al.: Turboelectric Aircraft Drive Key Performance Parameters and Functional Requirements. AIAA 2015–3890 (NASA/TM—2016-218919), 2015. http://ntrs.nasa.gov
3. Plas, A.P., et al.: Performance of a Boundary Layer Ingesting (BLI) Propulsion System. AIAA 2007–450, 2007.
4. Choi, Benjamin, et al.: Static Measurements on HTS Coils of Fully Superconducting AC Electric Machines for Aircraft Electric Propulsion System. AIAA 2017–4956, 2017.
5. Murphy, J.P., et al.: AC Loss in YBCO Coated Conductors at High dB/dt Measured Using a Spinning Magnet Calorimeter (Stator Testbed Environment). Cryogenics, vol. 86, 2017, pp. 57–69.
6. Lemmon E.W., et al.: NIST Standard Reference Database 23: Reference Fluid Thermodynamic and Transport Properties (REFPROP), Version 9.4. National Institute of Standards and Technology, Standard Reference Data Program, 2017.